REPORT DOCUMENTATION PAGE

Form Approved
OMB No. 0704-0188

PLEASE DO NOT RETURN YOUR FORM TO THE ABOVE ORGANIZATION.

1. REPORT DATE *(DD-MM-YYYY)*	2. REPORT TYPE	3. DATES COVERED *(From - To)*
04OCT2010	Final	15FEB2008 to 31MAY2010

4. TITLE AND SUBTITLE
(YIP-08) A NEW APPROACH TO MANIPULATING ELECTROMAGNETIC FIELDS: NEARFIELD FOCUSING PLATES

5a. CONTRACT NUMBER

5b. GRANT NUMBER
FA9550-08-1-0067

5c. PROGRAM ELEMENT NUMBER

6. AUTHOR(S)
ANTHONY GRBIC
UNIV OF MICHIGAN

5d. PROJECT NUMBER

5e. TASK NUMBER

5f. WORK UNIT NUMBER

7. PERFORMING ORGANIZATION NAME(S) AND ADDRESS(ES)
UNIV OF MICHIGAN/RESEARCH DEV & ADMIN
3003 SOUTH STATE STREET, 1058 WOLVERINE TOWER
ANN ARBOR, MI 48109-1274

8. PERFORMING ORGANIZATION REPORT NUMBER

9. SPONSORING/MONITORING AGENCY NAME(S) AND ADDRESS(ES)
AF OFFICE OF SCIENTIFIC RESEARCH
875 NORTH RANDOLPH STREET ROOM 3112
ARLINGTON VA 22203

10. SPONSOR/MONITOR'S ACRONYM(S)

11. SPONSOR/MONITOR'S REPORT NUMBER(S)

12. DISTRIBUTION/AVAILABILITY STATEMENT
UNLIMITED

13. SUPPLEMENTARY NOTES

14. ABSTRACT

The objective of this additional work effort is to provide compementary theory to the design of near-field plates with particular emphasis on reducing the reflection losses that earlier designs experienced. The PI and his new Postdoc will pursue the idea of adding magnetic dipoles/polarizabilities to the current design. The details of such dipole addition will be sorted out using a combination of analysis (including transformation optics) and numerics. The AF will benefit from having a device which can be utilized in wireless power transfer as well as in beam shaping for special antennas.

15. SUBJECT TERMS

16. SECURITY CLASSIFICATION OF:			17. LIMITATION OF ABSTRACT	18. NUMBER OF PAGES	19a. NAME OF RESPONSIBLE PERSON
a. REPORT	b. ABSTRACT	c. THIS PAGE			ANTHONY GRBIC
					19b. TELEPHONE NUMBER *(Include area code)* 734-647-1797

Near-Field Plates: Theory and Developement

Final Report for U.S Air Force Contract FA9550-08-1-0067
"A New Approach to Manipulating Electromagnetic Fields: Near-Field Focusing Plates"
PI: Anthony Grbic

Mohammadreza F. Imani and Anthony Grbic

October 4, 2010

Abstract

This report presents an in-depth investigation of near-field plates. Near-field plates are non-periodic, engineered surfaces that can focus electromagnetic field to subwavelength resolutions. Both numerical and analytical approaches are used to analyze and design these devices. The near-field plate concept is also expanded and used to design plates for near-field focusing/probing applications.

First, the step-by-step procedure used to design near-field plates is outlined. This is followed by an analytical investigation which illustrates the performance of near-field plates and highlights their characteristic features. Near-field plates are contrasted against other devices that can achieve subwavelength resolution field patterns. In addition, the first experimental near-field plate is reviewed. This initial near-field plate consisted of an array of printed interdigitated capacitors, and was able to focus microwave radiation emanating from a line source to a subwavelength near-field focal pattern.

In the remainder of the report, novel corrugated near-field plate designs are presented. First, a linearly corrugated plate is described. It consists of non-periodic, linear corrugations surrounding a central slit in a metallic surface. When excited through the slit, the near-field plate forms a one dimensional subwavelength near-field focal pattern. A design procedure is presented and full-wave simulation results are detailed which confirm the plate's ability to create a subwavelength focus. The effect of loss, edge diffraction, and frequency variations on the performance of the plate are studied. Two different methods of minimizing reflections from the plate are proposed. Furthermore, a linearly corrugated near-field plate design is fabricated and measured. Close agreement between experiment and simulation is demonstrated, verifying near-field plate's design and operation.

Next, a concentrically corrugated near-field plate is reported. It consists of non-periodic, concentric corrugations surrounding a coaxial aperture in a metallic surface. This plate is fed through the central coaxial aperture and forms a two dimensional subwavelength focal pattern. The procedure used to design the near-field plate is described, and full-wave simulation results verifying its ability to create a subwavelength focal spot are presented. Furthermore, the experimental performance of an impedance matched concentrically corrugated near-field plate is investigated. Experimental results confirm the near-field plate's superior ability to confine electromagnetic field, over that of a standard coaxial probe of equal dimensions. Lastly, preliminary experimental results are shown which demonstrate the super-resolving performance of a concentrically corrugated near-field plate serving as a near-field probe.

Finally, several application areas of near-field plates are identified. This final chapter explains how the ability to confine electromagnetic fields over an extended working distance can benefit areas ranging from near-field probing and microscopy to biomedical devices.

Contents

1.0

Introduction

The electromagnetic near field has intrigued scientists and engineers alike since the time Synge first proposed detecting the near field to obtain resolutions beyond the diffraction limit [1]. Synge showed that probing the near field (evanescent fields) of an object amounted to tapping into the object's subwavelength details. Nearly fifty years after Synge's proposal, Ash and Nicholls experimentally verified super-resolved near-field imaging in 1972 [2]. In near-field imaging, electrically-small probes such as tapered waveguide apertures as well as metallic and dielectric tips are used to obtain subwavelength resolution images [3, 4]. These probes provide high resolution by confining electromagnetic field to subwavelength dimensions. In order to obtain high resolutions, the imaged object must be placed extremely close to the probe, due to the strong divergence of radiation from the electrically-small aperture. However, high resolution at larger operating distances is desired in many applications. In order to achieve high resolution at extended near-field distances, the strong divergence of electromagnetic field from near-field probes needs to be overcome.

A decade ago, Pendry introduced the perfect lens as a candidate solution for overcoming the diffraction limit, and obtaining subwavelength resolutions at extended near-field focal lengths [5]. Pendry showed that a planar slab of negative refractive index metamaterial can manipulate the near field in such a way that it achieves perfect imaging, i.e., a perfect reconstruction of the source's near and far field. He also went on to show that P-polarized near field (evanescent field) could be focused with only a negative permittivity slab. Since that time, negative refractive index metamaterials have attracted strong interest. The experimental verification of negative refraction [6] and subwavelength focusing using negative refractive index [7], negative permittivity [8, 9], and negative permeability slabs [10] have demonstrated that near-field lenses are in fact a reality.

More recently, an alternative method of focusing electromagnetic waves to subwavelength resolutions was proposed [11, 12]. Specifically, a general class of aperture field distributions was introduced in [11], which can form a subwavelength focus at a prescribed focal plane in the aperture's reactive near field. This new approach to subwavelength focusing relies on patterned (grating-like) planar structures to produce the aperture fields needed to achieve a desired subwavelength focus. These planar structures, which have been referred to as near-field plates, can focus electromagnetic radiation to spots or lines of arbitrarily small subwavelength size. Moreover, they can be tailored to produce focal patterns of various shapes and symmetries.

Near-field plates provide a number of advantages over conventional near-field probes and metamaterial superlenses. The subwavelength focal pattern produced by the near-field plate can be tailored by simply patterning the plate's surface in different ways. This is not the case with conventional probes.

In addition, a near-field plate has a larger operating distance (focal length) than a conventional probe. Therefore, a given subwavelength resolution can be maintained at a greater distance than would be possible using a conventional probe. On the other hand, while near-field plates were originally inspired by negative index superlenses, their operation is distinct. Superlenses are bulk periodic structures, while near-field plates are non-periodic surfaces or arrays. As a result, near-field plates are much simpler to fabricate.

In [12], a systematic design procedure for near-field plates was described. The procedure allows one to design a plate that achieves a desired subwavelength focus along a focal plane in the plate's reactive near field. The design of the plate is dependent on both the source excitation as well as the desired subwavelength focal pattern. Further, it was proposed that completely passive near-field plates composed of inductive and capacitive elements could focus electromagnetic field to extreme subwavelength dimensions. As an example, a microwave realization of a near-field plate that focuses the field of a plane wave to a 1-dimensional (1-D) subwavelength focal pattern was reported in [12]. Full-wave electromagnetic simulations (Method of Moments) were presented that clearly demonstrated the plate's ability to overcome the diffraction limit. The effect of loss on the performance of near-field plates was also discussed and it was shown that practical losses have a minimal effect on a near-field plate's performance.

In this report, we investigate near-field plates as a possible solution for overcoming the diffraction limit and obtaining high resolution focal patterns at larger working distances. In the investigation, an analytical treatment of near-field plates is presented, which provides an intuitive understanding of their operation. Using this analytical treatment, distinct features of near-field plates and the differences between near-field plates and other similar structures such as metamaterial slabs and antenna arrays are explained. We also show how the initial near-field plate concept proposed in [11, 12] has been advanced to develop more practical near-field plate realizations. These novel realizations are studied, and their design and operation are described. The design procedure is verified through full-wave simulation and experimental results. Finally, applications of near-field plates in various areas are discussed. As an example, preliminary experimental results verifying the near-field plate's ability to serve as a high resolution near-field probe are reported.

This report is organized into five chapters. In the next chapter, we review the procedure for designing near-field plates as well as their principle of operation. An analytical description of near-field plates is presented that provides insight into their operation [13]. Closed form expressions for the near-field plate aperture field, current density, and impedance profile are derived. Characteristic features of a near-field plate's aperture field and current density are discussed. Furthermore, the experimental performance of the initial near-field plate is presented [14, 15]. It is shown that a near-field plate consisting of an array of interdigitated capacitors can focus 1.027 GHz microwave radiation emanating from an S-polarized cylindrical source to a focus with full width at half maximum (FWHM) of $\lambda/18$, where λ is the free space wavelength.

In the third chapter, an alternative near-field plate implementation is reported. This novel near-field plate consists of a central slit in a metallic plate surrounded with non-periodic linear corrugations. The structure, referred to as a linearly corrugated near-field plate [16], is fed through the central slit. The non-periodic corrugations are designed to tailor the radiation emanating from the slit to a prescribed subwavelength focus. A design procedure for this structure is presented and verified through full-wave simulation. It is shown that this structure is robust to practical losses and can be impedance matched. Finally, an experimental verification of the linearly corrugated near-field plate is presented [17].

In the fourth chapter, we explore a high resolution near-field probe based on a near-field plate. The probe consists of non-periodic, concentric corrugations that surround a central coaxial aperture in a

metallic surface [18]. This structure, referred to as concentrically corrugated near-field plate, is fed through the central coaxial aperture. It is capable of producing a 2-dimensional (2-D) subwavelength focus. A design procedure for this structure is outlined and the structure is thoroughly investigated through full-wave simulation. In addition, experimental results that confirm the performance of this near-field plate are reported [19, 20]. In the experiments, electric-field focal patterns formed by the near-field plate are compared to those created by a conventional coaxial probe of the same dimensions, and are shown to be significantly narrower. In addition, the concentrically corrugated near-field plate is used as a probe to image two closely spaced dipole sources. The near-field plate probe achieves images with significantly higher resolution compared to the conventional coaxial probe.

In the final chapter, the results presented in this report are summarized. Advantages and disadvantages of near-field plates compared to other similar structures are discussed. Application areas of near-field plates such as near-field probing, data storage, as well as biomedical devices are described [21].

Lastly, it should be noted that the near-field plate concept has also inspired others to develop similar subwavelength focusing devices. For example, devices termed holography-inspired screens and spatially beam-shifted transmission screens, have been pursued in [22–24]. Since a near-field plate's design and operation are frequency independent, they can also be designed at higher frequencies. For example, theoretical near-field plates at optical wavelengths have been proposed in [25–28].

2.0

Near-Field Plates: Analytical and Numerical Modeling, and Experimental Verification

2.1 Introduction

A step-by-step procedure for designing near-field plates was first outlined in [12]. This design procedure relied on solving an electromagnetic inverse problem through numerical simulation (Method of Moments). It was demonstrated that a near-field plate can be realized using purely reactive surface impedances. As an example, a near-field plate consisting of an array of capacitors was shown in simulation to focus a plane wave to a subwavelength resolution focal pattern. The design was shown to be robust to practical losses.

While the numerical approach outlined in [12] is sufficient for design purposes, it does not provide sufficient intuition into the operation and the performance of near-field plates. Here, we characterize near-field plates analytically in order to gain insight into their operation and design. In this analytical treatment, closed-form expressions for the currents excited on a near-field plate, as well as its impedance profile are derived. In addition, spectral domain representations of the current density and the electric field at the surface of the plate are studied. Both the spatial domain and spectral domain studies are used to highlight the performance of near-field plates.

After the performance and operation of a near-field plate is thoroughly explained, the first experimental near-field plate is presented. The plate is designed following the procedure outline in [12] and consists of an array of interdigitated capacitors. In the experiments, the fabricated near-field plate is shown to focus 1.027 GHz microwave radiation, emanating from an S-polarized cylindrical source, to a focus with $\mathrm{FWHM} = \lambda/18$, where λ is the free space wavelength. Close agreement between measurement and simulation is demonstrated, thereby verifying the near-field plate's design and operation.

In this chapter, the near-field plate design procedure is first reviewed. The plate is assumed to be infinite in width to simplify the analytical treatment. In the analytical treatment, the current density on the plate is found in the spectral domain and then inverse Fourier transformed to obtain its spatial dependence, as well as the plate's impedance profile [13]. The analytically derived expressions are then compared to those computed numerically for electrically-wide plates, in order to validate the analytical approach. Finally, the experimental near-field plate is presented. Its design parameters are listed and the measurement setup is described in detail. Both experimental and simulation results confirming the near-field plate's ability to form subwavelength focal patterns are reported.

2.2 Near-Field Plate Design Procedure

The near-field plate configuration considered in the analytical investigation is depicted in Figure 2.1. The plate is located along the $z = 0$ plane (sheet plane) and the focal plane is assumed to be the $z = L$ plane, where L is the focal length. Furthermore, the electromagnetic fields are assumed to be polarized and invariant in the x direction (S-polarized). In this discussion, the electric field along the focal plane will be referred to as the focal pattern, while the electric field along the surface of the plate will be referred to as E_{total}. We will investigate a near-field plate that produces a subwavelength focal pattern of the following form,

$$\vec{\mathbf{E}}(y, z = L) = jM|E_{max}|e^{-qL}qL\text{sinc}(qy)\hat{x} \tag{2.1}$$

where $L = \lambda/16$, $q = 10k$ and k is the free space wavenumber at the operating frequency $f = 1.0$ GHz. Also $M = 6$ is a real constant known as the amplification factor, which expresses the focal pattern in terms of the maximum of the incident electric field at the surface of the plate: $|E_{max}| = |E_{inc}(y = 0)|$. These values for L, q, f, and M are assumed throughout the analytical investigation. As explained in [12], the imaginary number j ensures that the plate's surface impedance is primarily reactive. For the assumed parameters, the sinc focal pattern and its spectrum are shown in Figure 2.2. The constant q represents the maximum transverse wavenumber $k_y = q$ that contributes to the focal pattern, and as a result determines its null-to-null beamwidth, $2\pi/q = \lambda/10$. Finally, the plate is assumed to be electrically thin in the z direction ($\lambda \gg$ thickness) so that current densities in the direction normal to the plate can be neglected, and the plate can be modeled as a sheet characterized by a surface impedance $\eta_{sheet}(y)$ [29].

The first step to designing this near-field plate involves finding the electric field, $E_{total}(y)$, that is needed at the surface of the plate to produce the focal pattern [12]. By back-propagating the focal pattern given in Equation (2.1), $E_{total}(y)$ can be easily obtained through an inverse Fourier transform (IFT):

$$\vec{\mathbf{E}}_{total}(y) = \mathcal{F}^{-1}\{\vec{\mathbf{E}}_{total}(k_y)\} = jM|E_{max}|\mathcal{F}^{-1}\{\pi Le^{(-q+jk_z)L}\Pi(k_y, q)\}\hat{x} \tag{2.2}$$

where the symbol $\mathcal{F}^{-1}$ denotes the IFT with respect to transverse wavenumber k_y; $\Pi(k_y, q)$ is a rectangular function in the spectral domain with amplitude equal to one extending from $k_y = -q$ to $k_y = q$; and k_z is the wavenumber in the z direction defined as:

$$k_z = \begin{cases} \sqrt{k^2 - {k_y}^2} & : \quad {k_y}^2 < k^2 \\ -j\sqrt{{k_y}^2 - k^2} & : \quad {k_y}^2 > k^2. \end{cases} \tag{2.3}$$

Since the configuration is two dimensional and the electric fields and current densities only have x components, the scalar form of these quantities with a subscript x will be used. Figures 2.3 and 2.4 show the spectral $E_{total}(k_y)$ and spatial $E_{total}(y)$ computed in this manner. It should be noted that the numerically computed values for $E_{total}(y)$ that are used here are different from those in [12], where an approximate analytical expression for $E_{total}(y)$ was used.

The second design step involves finding the current density $J_x(y)$ on the plate that produces $E_{total}(y)$. The current density can be computed by solving the following integral equation [12]:

$$E_{inc}(y) - \frac{k\eta}{4}\int_{\frac{-W}{2}}^{\frac{W}{2}} J_x(y')H_0^{(2)}(k|y - y'|)dy' = E_{total}(y) \tag{2.4}$$

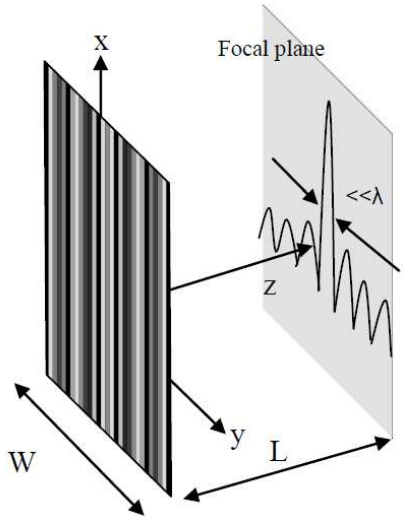

Figure 2.1: A schematic showing the near-field plate ($z = 0$) and focal plane ($z = L$). A near-field plate is a non-periodically patterned, planar structure that can focus electromagnetic radiation to lines or spots of arbitrary subwavelength dimension (form [13]).

which represents the boundary condition at the plate's surface. The field quantity $E_{inc}(y)$ denotes the electric field incident on the plate from an external source, $H_0^{(2)}$ is the zeroth order Hankel function of the second kind, $\eta = 120\pi\Omega$ is the free space wave impedance, and W is the width of the near-field plate. Substituting Equation (2.2) into Equation (2.4) yields an integral equation which can be solved to find $J_x(y)$.

Once $J_x(y)$ is known, $\eta_{sheet}(y)$ can be computed by simply taking the ratio of $E_{total}(y)$ to $J_x(y)$:

$$\eta_{sheet}(y) = \frac{E_{total}(y)}{J_x(y)}. \tag{2.5}$$

In order to find $J_x(y)$ and subsequently $\eta_{sheet}(y)$, Equation (2.4) was solved numerically in [12]. In this section, we solve Equation (2.4) analytically, to obtain approximate closed-form expressions for both $J_x(y)$ and $\eta_{sheet}(y)$ [13]. In the analytical treatment, we assume that the plate is infinitely wide, in order to simplify the integral on the left hand side of Equation (2.4) to a convolution:

$$E_{inc}(y) - \frac{k\eta}{4}\int_{-\infty}^{\infty} J_x(y')H_0^{(2)}(k|y-y'|)dy' = jM|E_{max}|\mathcal{F}^{-1}\{\pi L e^{(-q+jk_z)L}\Pi(k_y,q)\}. \tag{2.6}$$

Since the convolution becomes a multiplication in the spectral domain, an expression for $J_x(k_y)$ can be found in the spectral domain and then inverse Fourier transformed to obtain approximate expressions for $J_x(y)$ and $\eta_{sheet}(y)$. The Fourier transform properties of Hankel and Bessel functions as well as their integral representations [29–31] are utilized in deriving the approximate expressions. Although we consider a near-field plate under a specific excitation (i.e. cylindrical wave), the analytical approach presented here can be applied to near-field plates designed for arbitrary incident waves and desired focal patterns, provided that the Fourier transformation of the incident and desired focal patterns are known.

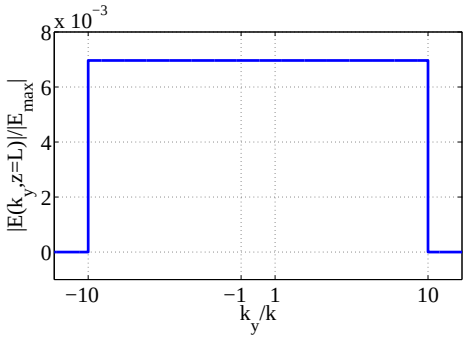

(a) Spectral representation

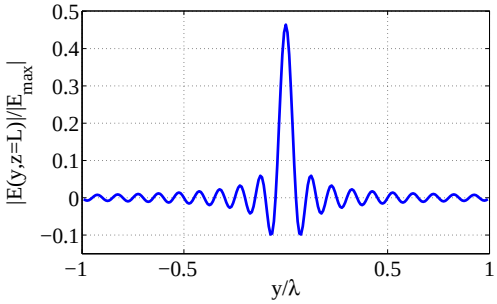

(b) Spatial representation

Figure 2.2: Spectral and spatial representation of the electric-field focal pattern ($\vec{\mathbf{E}}$) given by Equation (2.1) (form [13]).

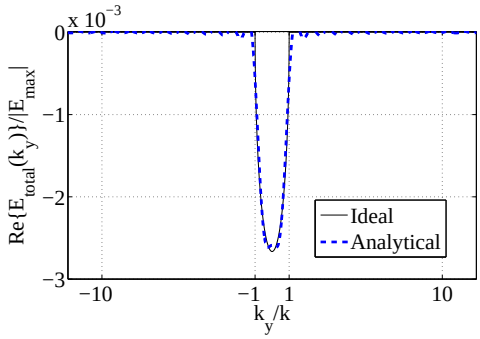

(a) Real part

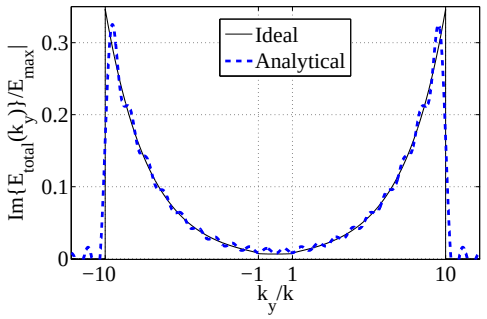

(b) Imaginary part

Figure 2.3: Spectral representation of the electric field at the surface of the plate. The solid line represents $E_{total}(k_y)$ given by Equation (2.2). The dashed line is the spectral domain representation of the approximate $E_{total}(y)$ given by Equation (2.17). The ripples are due to the truncation of the numerical Fourier transform (Gibb's phenomena) (form [13]).

2.3 Focusing with Infinitely-Wide Near-Field Plates: Analytical Formulation

A near-field plate is considered that can focus a cylindrical wave to a subwavelength focal pattern given by Equation (2.1). The source of the cylindrical wave will be an x-directed electric line source with current I located at $(y = 0, z = -d)$. Throughout this section, it will be assumed that $I = 1$ mA and $d = \lambda/16$. The electric field produced by the line source at the plate's surface is [30]:

$$E_{inc}(y) = -\frac{k\eta I}{4} H_0^{(2)}(k\sqrt{y^2 + d^2}) \tag{2.7}$$

Substituting $E_{inc}(y)$ into the integral equation (2.6) yields:

$$-\frac{k\eta I}{4} H_0^{(2)}(k\sqrt{y^2 + d^2}) - \frac{k\eta}{4} \int_{-\infty}^{\infty} J_x(y') H_0^{(2)}(k|y - y'|) dy' = jM|E_{max}|\mathcal{F}^{-1}\{\pi L e^{(-q+jk_z)L} \Pi(k_y, q)\}. \tag{2.8}$$

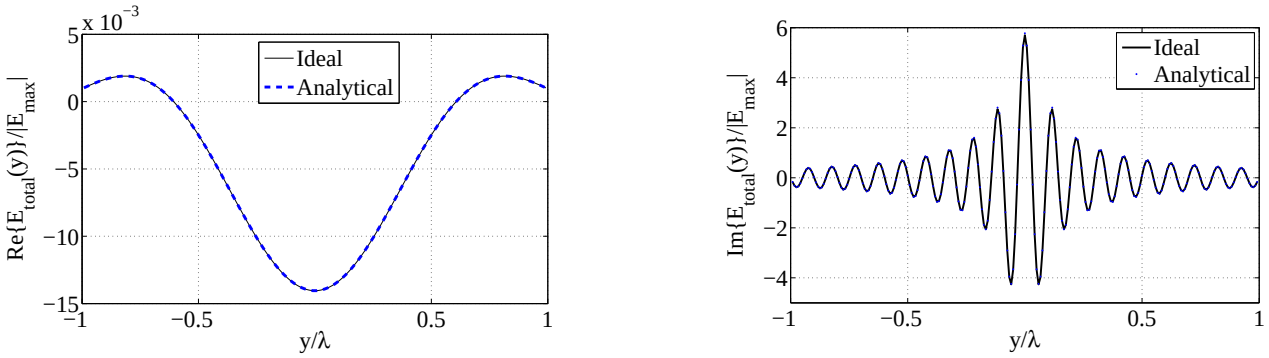

(a) Real part

(b) Imaginary part

Figure 2.4: Spatial representation of the electric field at the surface of the plate. The solid line represents $E_{total}(y)$ given by Equation (2.2) while the dashes in (a) and the dotted line in (b) represents the analytical expression given by Equation (2.17) (form [13]).

This integral equation can be Fourier transformed exactly to obtain its spectral domain counterpart:

$$-\frac{k\eta I}{2}\frac{e^{(-jk_z d)}}{k_z} - \frac{k\eta}{2}\frac{J_x(k_y)}{k_z} = j\pi M|E_{max}|Le^{(-q+jk_z)L}\Pi(k_y,q) \tag{2.9}$$

By rearranging Equation (2.9), the following expression for the spectral domain $J_x(k_y)$ can be obtained:

$$J_x(k_y) = J_x^{inc}(k_y) + J_x^{foc}(k_y) = -Ie^{(-jk_z d)} - \frac{j2\pi LM|E_{max}|e^{(-q+jk_z)L}k_z}{k\eta}\Pi(k_y,q) \tag{2.10}$$

Equation (2.10) reveals that the current density on the near-field plate consists of two parts. The first term, referred to as $J_x^{inc}(k_y)$, cancels the incident cylindrical wave in the region $z > 0$, while the second term, referred to as $J_x^{foc}(k_y)$, forms the desired focal pattern. The first term, J_x^{inc}, can be inverse Fourier transformed directly:

$$J_x^{inc}(y) = \frac{jkdI}{2\sqrt{d^2+y^2}}H_1^{(2)}(k\sqrt{d^2+y^2}) \tag{2.11}$$

The real and imaginary parts of the IFT of $J_x^{foc}(k_y)$ are found separately. The IFT of the imaginary part of $J_x^{foc}(k_y)$ is found exactly, by transforming the propagating spectrum ($|k_y| < k$) of $J_x^{foc}(k_y)$, and retaining its imaginary part:

$$Im\{J_x^{foc}(y)\} = -\frac{\pi ML|E_{max}|ke^{-qL}}{2\eta}[J_0(k\sqrt{y^2+L^2}) + \frac{y^2-L^2}{y^2+L^2}J_2(k\sqrt{y^2+L^2})] \tag{2.12}$$

where J_0 and J_2 denote Bessel functions of the first kind. The real part of $J_x^{foc}(y)$ can be derived approximately. Given that the second term of Equation (2.10) increases exponentially as a function of k_y for $|k_y| \gg k$, we apply the following quasi-static approximation,

$$\sqrt{k^2-k_y^2} \approx -j|k_y|. \tag{2.13}$$

Under this assumption, the real part of $J_x^{foc}(k_y)$ simplifies to:

$$Re\{J_x^{foc}(k_y)\} \approx \frac{-2\pi LM|E_{max}|e^{(-q+|k_y|)L}|k_y|\Pi(k_y,q)}{k\eta}. \tag{2.14}$$

The quasi-static approximation is valid when $q \gg k$, in other words for near-field plates that focus electromagnetic waves to extremely subwavelength resolutions. It should be noted that the growing nature for $Re\{J_x^{foc}(k_y)\}$ is expected, since it results from restoring/amplifying the evanescent electric field from the focal plane ($z = L$) to the sheet plane ($z = 0$) (see Figure 2.3(b)). Inverse Fourier transforming Equation (2.14), leads to the following approximate expression for the real part of $J_x^{foc}(y)$,

$$Re\{J_x^{foc}(y)\} \approx -\frac{2ML|E_{max}|}{k\eta(L^2+y^2)}[(Lq - \frac{L^2-y^2}{L^2+y^2})\cos(qy) + (yq - \frac{2Ly}{L^2+y^2})\sin(qy)] \tag{2.15}$$

By combining Equations (2.12) and (2.15), the following expression for $J_x(y)$ is obtained:

$$\begin{aligned} J_x(y) = \frac{jkdI}{2\sqrt{d^2+y^2}}H_1^{(2)}(k\sqrt{d^2+y^2}) - \frac{j\pi M|E_{max}|Lke^{-qL}}{2\eta}[J_0(k\sqrt{y^2+L^2}) + \frac{y^2-L^2}{y^2+L^2}J_2(k\sqrt{y^2+L^2})] \\ -\frac{2M|E_{max}|L}{k\eta(L^2+y^2)}[(Lq - \frac{(L^2-y^2)}{L^2+y^2})\cos(qy) + (yq - \frac{2Ly}{L^2+y^2})\sin(qy)]. \end{aligned} \tag{2.16}$$

The accuracy of Equation (2.16) can be verified by comparing its numerical Fourier transform, to the exact expression for $J_x(k_y)$ given by Equation (2.10). The two plots are compared in Figure 2.5 and show close agreement. The ripples at the sharp transitions are due to the truncation of the numerical Fourier transform (Gibb's phenomena).

Finally, in order to have a completely analytical expression for η_{sheet}, we must find a closed-form expression for $E_{total}(y)$. In [12], an analytical expression for $E_{total}(y)$ was derived which we will use here with a slight modification:

$$\begin{aligned} E_{total}(y) = jM|E_{max}|L[\frac{L\cos(qy) + y\sin(qy)}{L^2+y^2} + 2\pi qe^{(-qL)}(\cos(kL)-1)\mathrm{sinc}(qy)] \\ -\frac{\pi L^2 e^{-qL}kM|E_{max}|}{2\sqrt{L^2+y^2}}J_1(k\sqrt{L^2+y^2}). \end{aligned} \tag{2.17}$$

The first term is the same as the formula used in [12], and can be derived under the quasi-static approximation Equation (2.13). The second term is a modification factor which is included to match the approximate expression for $E_{total}(k_y)$ with its exact value at $k_y = 0$. The third term is the real part of $E_{total}(y)$ resulting from the propagating spectrum ($|k_y| < k$). The analytical expressions for $E_{total}(k_y)$ and $E_{total}(y)$ are compared to the numerically computed ones in Figures 2.3 and 2.4, and show close agreement. Now that a closed-form expression for the current density and E_{total} on the infinitely-wide plate are known, the plate's sheet impedance can be found by substituting Equations (2.16) and (2.17) into Equation (2.5). Figures 2.3 and 2.5 reveal that the imaginary part of the current density $J_x(y)$ and the real part of $E_{total}(y)$ are much smaller than their real and imaginary counterparts, respectively. This fact explains why only the reactive part of sheet impedance $Im\{\eta_{sheet}(y)\}$ is typically used in the implementation of practical near-field plates.

2.4 Focusing with Finite Near-Field Plates: Analytical vs. Numerical

In the previous section, we derived the current density and impedance for an infinitely-wide near-field plate that focuses a cylindrical wave to a subwavelength focus (line focus). In this section, we compare

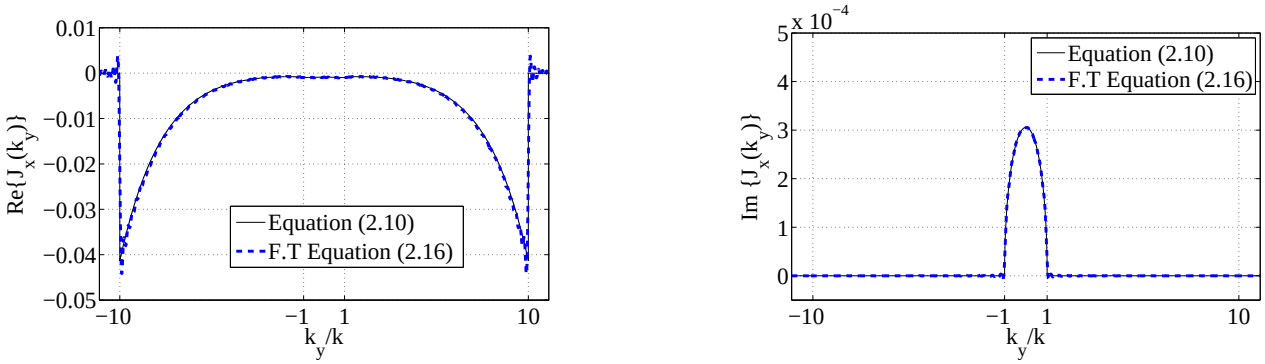

(a) Real part

(b) Imaginary part

Figure 2.5: The (a) real and (b) imaginary parts of the spectral representation of the current density $J_x(k_y)$. The solid line represents Equation (2.10) and the dashed line represents the numerical Fourier transform of Equation (2.16) (form [13]).

the analytical results to numerical results for a finite plate that is $W = 10\lambda$ wide (electrically-wide). The Method of Moments (MoM) is used to simulate the finite-width plate. To be precise, the point matching method is employed with a discretization of $\lambda/40$. The current densities obtained analytically and numerically are depicted in Figure 2.6. They match up well, other than the slight differences near the edges of the finite plate that result from edge diffraction. It should be noted that the analytical expression for $Re\{J_x(y)\}$ has been derived based on the quasi-static assumption (Equation (2.13)), which is valid for $q \gg k$. For larger focal spots, or equivalently smaller values of q, it becomes less valid. As a rule of thumb, the quasi-static assumption holds for $q > 3k$.

Equations (2.16) and (2.17) and Figures 2.3, 2.4, 2.5, and 2.6 illustrate a distinctive feature of the near-field plates. The current density and also the electric field on the surface of the near-field plate exhibits an evanescent spectrum that increases with increasing values of k_y (see Figures 2.3 and 2.5). This evanescent spectrum results in a highly oscillatory spatial domain counterpart with rapid variations in the phase of adjacent elements (see Figures 2.4 and 2.6 and Equation (2.16)). The evanescent spectrum produced by the near-field plate is similar to the enhanced evanescent spectrum observed at the exit surface of a negative refractive index metamaterial slab. However, the process by which the evanescent spectrum is enhanced by near-field plates is quite different from that for metamaterial slabs. Negative refractive index metamaterials, which are periodic bulk media, enhance the evanescent spectrum through the interaction of surface plasmons, while near-field plates are non-periodic planar structures which achieve an enhanced evanescent spectrum through a modulation of their surface reactance. Finally, it should be emphasized that the enhanced evanescent spectrum is required to form the subwavelength focal pattern. The spectrum of the subwavelength focal pattern consists of an extended evanescent spectrum ($|k_y| > |k|$) (see Figure 2.2 (a)). The evanescent spectrum decays as the field propagates to the focal plane with the larger wavenumbers experiencing a higher rate of decay. Therefore, the field at the surface of the near-field plate must have a growing evanescent spectrum with respect to k_y to compensate for the higher decay rate associated with the larger wavenumbers.

The focal patterns, produced by both the analytical and numerical current densities, were computed

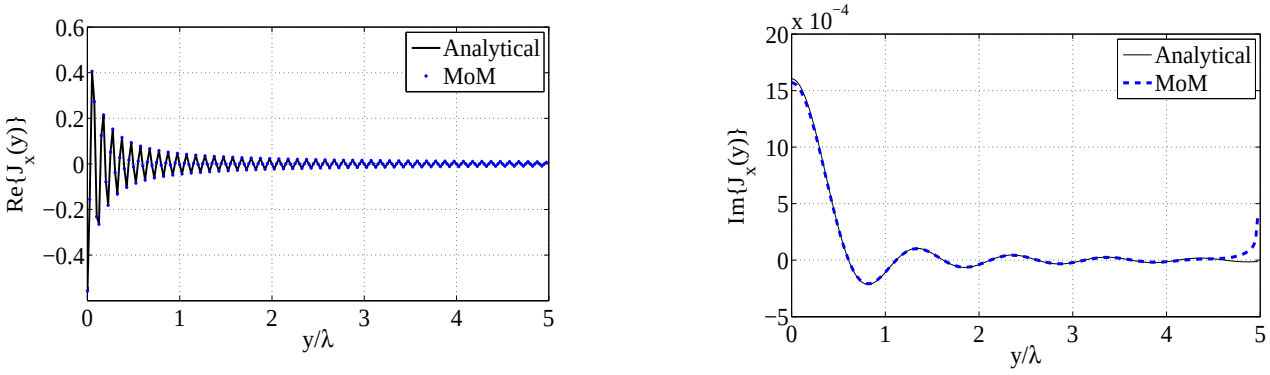

(a) Real part

(b) Imaginary part

Figure 2.6: The (a) real and (b) imaginary parts of the current density $J_x(y)$. The solid line represents the analytically derived current density given by Equation (2.16). The dots in (a) and the dashed line in (b) represent the numerically (MoM) computed current density. The current density is only shown on half of the plate since it is symmetric about $y = 0$ (form [13]).

using the two dimensional free space Green's function [30],

$$E_x(y, z = L) = -\frac{k\eta I}{4} H_0^{(2)}(k\sqrt{y^2 + (d + L)^2}) - \frac{k\eta}{4} \int_{\frac{-W}{2}}^{\frac{W}{2}} J_x(y') H_0^{(2)}(k\sqrt{(y - y')^2 + L^2}) dy' \quad (2.18)$$

and are plotted in Figure 2.7. The focal patterns produced by the analytically derived current density show close agreement with those computed using the MoM. Furthermore, 2-D plots of the vertical electric field computed using the analytically derived and numerically computed current densities (J_x) are shown in Figure 2.8. The incident electric field excites a highly oscillatory field on the surface of the plate ($z = 0$). This highly oscillatory field forms a narrow beam for ($0 < z < L$) which converges to the subwavelength focus along the focal plane. Beyond the focal plane ($z > L$), the field diverges rapidly. The ability of the near-field plate to maintain a narrow beam over its focal length ($0 < z < L$) is an interesting feature which can be used in many applications to increase operating distance while keeping resolution high. Later in this chapter, and also in chapters 3 and 4, this feature will be demonstrated through experiments and its applications will be discussed in more detail. Figure 2.8 also shows reflection from the plate in the region $z < 0$. In the following chapters, methods to decrease reflection from near-field plates will be presented.

Finally, since one of the main goals was to find an expression for the plate's sheet impedance, the reactive sheet impedance resulting from both methods is plotted in Figure 2.9. Impedance values for a 4λ plate are shown, since it is simpler to implement than a plate that is 10λ wide. Given that only the reactive part of the sheet impedance is used in the realization of near-field plates [12], the reactive part is only shown. The impedances show good agreement over the majority of the plate with the exception of the plate's edges.

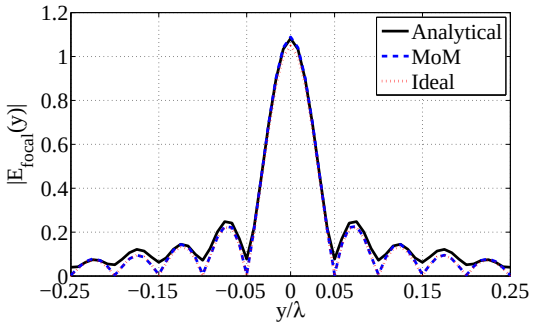

Figure 2.7: Close-up view of the magnitude of electric field at the focal plane. The solid line represents the electric field at the focal plane produced by the analytically derived current density given by Equation (2.16). The dashed line represents the electric field at the focal plane produced by the numerically computed (MoM) current density. The dotted line represents the ideal focal pattern given by Equation (2.1) (form [13]).

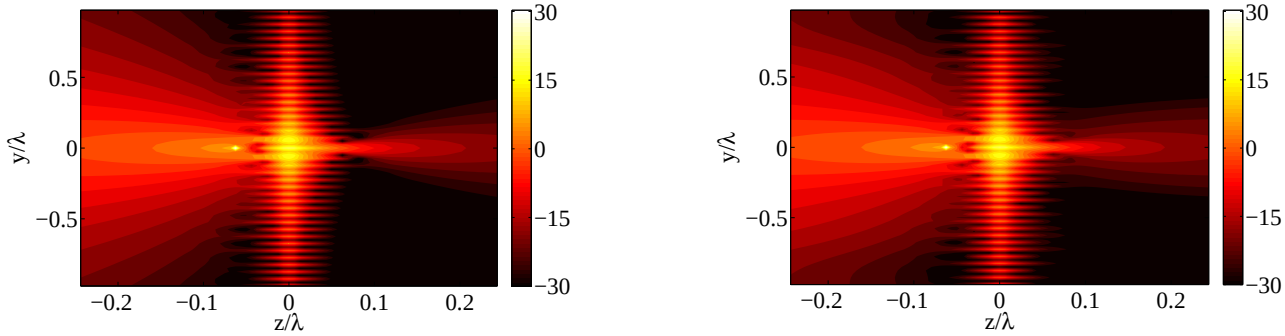

(a) MoM

(b) Analytical

Figure 2.8: 2-D plots of the vertical electric field (in dB) surrounding the 10λ near-field plate. The electric field is computed for the current densities obtained (a) numerically (MoM) and (b) analytically (form [13]).

2.5 An Experimental Near-Field Plate

The experimental near-field plate presented here is similar to the one discussed in the analytical investigation. In practice, the plate's width (the plate's dimension along y-axis in Figure 2.1) has to be finite. In this experimental near-field plate [14], the width was chosen to be $W = \lambda$, where $\lambda = 30$ cm, corresponding to a 1.0 GHz frequency of operation. The plate is illuminated with a cylindrical source located at distance $d = \lambda/15$ from the plate, and the focal plane is located at a distance $L = \lambda/15$ on the opposite side of the plate. In order to emulate an infinite height (the plate's dimension along x-axis in Figure 2.1), the near-field plate is placed within a parallel-plate waveguide environment (a 2-D scattering chamber). By image theory, the top and bottom ground planes act as mirrors and make the finite-height ($H_c \approx \lambda/20$) near-field plate and the source appear as if they were infinite in the x direction.

The plate is designed following the procedure described in [12]. A subwavelength sinc function focal pattern, similar to the one used in the analytical investigation (see equation (2.1)), is assumed. By back-propagating the focal pattern, the required total field on the surface of the plate is approximately

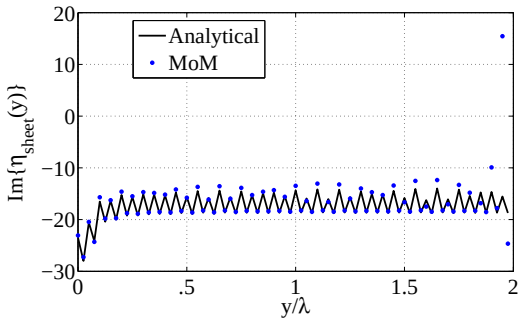

Figure 2.9: The reactive sheet impedance, $Im\{\eta_{sheet}(y)\}$. The solid line represents the analytically derived $Im\{\eta_{sheet}(y)\}$ using Equations (2.16) and (2.17) in Equation (2.5). The dots represent the numerically computed $Im\{\eta_{sheet}(y)\}$ using MoM. The surface impedance is only shown for half of the plate since it is symmetric about $y = 0$ (form [13]).

obtained:

$$E_{total}(y) = jM|E_{max}|L[\frac{L\cos(qy) + y\sin(qy)}{L^2 + y^2} \tag{2.19}$$

This expression is similar to Equation (2.17) but the second and the third terms are neglected. For this particular near-field plate design, the amplification factor is set to $M = 2$ and $q = 10k$ to yield $\mathrm{FWHM} = \lambda/20$. To emulate a continuously varying surface impedance, the plate is discretized into $n = 39$ separate elements of width $W_c \approx \lambda/40$ and height $H_c \approx \lambda/20$. Given the dimensions above, the required surface impedance (η_{sheet}) is obtained. The impedance of each element (Z_{sheet}) is determined using the properly normalized surface impedance (η_{sheet}) evaluated at the center of each strip:

$$Z_{sheet}(n) = \eta_{sheet}(n)\frac{H_c}{W_c}. \tag{2.20}$$

The impedance elements found through this procedure are listed in Table 2.1 and are all capacitive. This is expected given that the mutual impedance matrix defining the electromagnetic interaction between the impedance elements is predominantly inductive for S-polarized radiation. These inductive mutual impedances resonate with the capacitive impedances Z_{sheet}, and result in an aperture field that is $M = 2$ times higher in amplitude than the field incident on the plate.

The designed near-field plate is implemented as an array of interdigitated copper capacitors printed on a $127\ \mu\mathrm{m}$ thick Rogers RO3003 microwave substrate with permittivity $\epsilon_r = 3.00 \pm 0.04$ and loss tangent $\tan\delta = 0.0013$. The impedances $Z_{sheet}(n)$ are realized as individual interdigitated capacitors (see Figure 2.10). To implement the required capacitances, the length of the capacitive fingers is adjusted between $3.556\ \mathrm{mm}$ and $13.868\ \mathrm{mm}$, while keeping the finger widths and the gaps between the fingers constant at $229\ \mu\mathrm{m}$ and $127\ \mu\mathrm{m}$, respectively. The interdigitated capacitors are optimized using the commercial finite element electromagnetic solver Ansoft HFSS. The fourth column of Table 2.1 lists the heights of the capacitive fingers that are used to realize each of the impedance elements. The third column of Table 2.1 lists the impedances obtained from scattering simulations at $1.0\ \mathrm{GHz}$ performed using Ansoft HFSS (Z_{21}). A comparison of columns two and three of Table 2.1 shows that the extracted impedances closely match the desired ones.

The fabricated near-field plate was measured in the setup shown in Figure 2.11. In this setup, the microwave source is a coaxially-fed thin wire dipole antenna, which acts as a vertical line current. The

n	Z_{sheet}	Z_{21}	Finger Height (mm)
0	$-53.010i$	$-52.064i$	6.401
1	$-95.093i$	$-93.518i$	3.556
2	$-36.032i$	$-35.251i$	9.246
3	$-42.487i$	$-41.433i$	7.874
4	$-35.834i$	$-35.116i$	9.296
5	$-42.955i$	$-42.825i$	7.772
6	$-28.686i$	$-27.555i$	11.582
7	$-37.328i$	$-36.977i$	8.915
8	$-32.142i$	$-31.404i$	10.338
9	$-38.575i$	$-38.043i$	8.687
10	$-27.881i$	$-26.714i$	11.913
11	$-36.823i$	$-35.880i$	9.017
12	$-29.521i$	$-28.645i$	11.252
13	$-36.945i$	$-35.880i$	9.017
14	$-29.531i$	$-28.645i$	11.252
15	$-37.339i$	$-36.977i$	8.915
16	$-25.027i$	$-22.405i$	13.868
17	$-35.196i$	$-34.628i$	9.449
18	$-50.230i$	$-49.634i$	6.706
19	$-54.354i$	$-53.572i$	6.223

Table 2.1: Characteristics of the capacitive elements of the first experimental near-field plate reported in [14].

outer conductor of the coaxial feed is attached to the bottom ground plane while the center conductor, which acts as the dipole antenna, is attached to the top ground plane. This coaxially-fed antenna is connected to the port of a Hewlett-Packard 8753D vector network analyzer (VNA). Connected to the second port is an electric field probe made from a 0.086 inch semi-rigid coaxial cable. This probe is inserted through a horizontal slit cut into the absorber on the image side of the parallel-plate waveguide opposite to the near-field plate. To detect the x-polarized electric field, the center conductor of the horizontal probe is extended and bent in the vertical direction. By roster scanning the probe within the parallel-plate waveguide using a two-axis translation stage, the phase and magnitude of the vertical electric field on the image side of the near-field plate are recorded.

Figures 2.12 (A) and (B) show contour plots of the experimental and calculated electric field. The plots show very good agreement between the measurements and finite element simulations. The simulations took into account all electromagnetic interactions as well as the losses associated with the finite conductivity of the capacitors. The relative magnitude of the electric field contour is the same for both plots and the minima and maxima of the highly oscillatory field between the plate and focal plane show very good agreement between simulation and experiment. It should be noted that the operating frequency of the fabricated near-field plate is 1.027 GHz, which is 2.7% higher than the simulation frequency, 1.0 GHz. This frequency difference is consistent with etching tolerances associate with the fabrication of the near-field plate as well as variations in the parallel plate waveguide height in which it is tested.

Figure 2.12 (C) compares the simulated and measured electric field intensity along the focal plane,

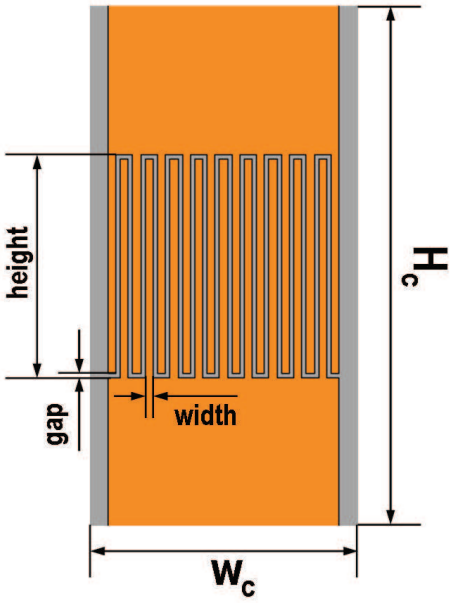

Figure 2.10: A unit cell of the near-field plate reported in [14]. Each unit cell consists of a printed interdigitated capacitor with dimensions: $H_c = 15.0$ mm, $W_c = 7.5$ mm, gap=127 μm, width=229 μm.

denoted as *Experiment* and *Simulation* respectively. The *Experiment* and *Simulation* plots show close agreement. The main peaks in the two plots exhibit $\mathrm{FWHM} = \lambda/18$. To emphasize the narrowness of the focus, an additional curve has been plotted illustrating what the beamwidth of the electric field would be if the near-field plate was not present and is denoted as *No plate*. The *No plate* plot exhibits a $\mathrm{FWHM} = \lambda/2.78$ which is 6.47 times wider than the focal pattern produced by the near-field plate.

Finally, the frequency response of the plate is shown in Figure 2.13. The resolution (FWHM of the focus) decreases from its narrowest value of $\lambda/20.0$ at 1.025 GHz to $\lambda/9.3$ at 1.065 GHz . At frequencies below 1.025 GHz, the focal pattern exhibited multiple peaks.

2.6 Conclusion

In this chapter, we have analytically modeled and characterized near-field plates. Expressions for the induced current density and surface impedance of infinitely-wide plates were found. Further, it was shown that the expressions obtained for infinitely wide plates can be used to approximate the characteristics of finite-width plates. In fact, we have shown that the current density on a near-field plate can be split into two parts. One part cancels the incident wave on the focus-side of the plate, while the other part produces the desired subwavelength focal pattern. This chapter also mathematically demonstrated why only the reactive part of a near-plate's sheet impedance can be used in their design. Finally, a near-field plate was designed and fabricated using an array of interdigitated capacitors. The fabricated plate was shown in experiment to focus 1.027 GHz emanating from an S-polarized cylindrical source to focus with $\mathrm{FWHM} = \lambda/18$. Close agreement between measurement and simulation results were demon-

strated, thereby confirming the feasibility of implementing passive surfaces that can focus microwave

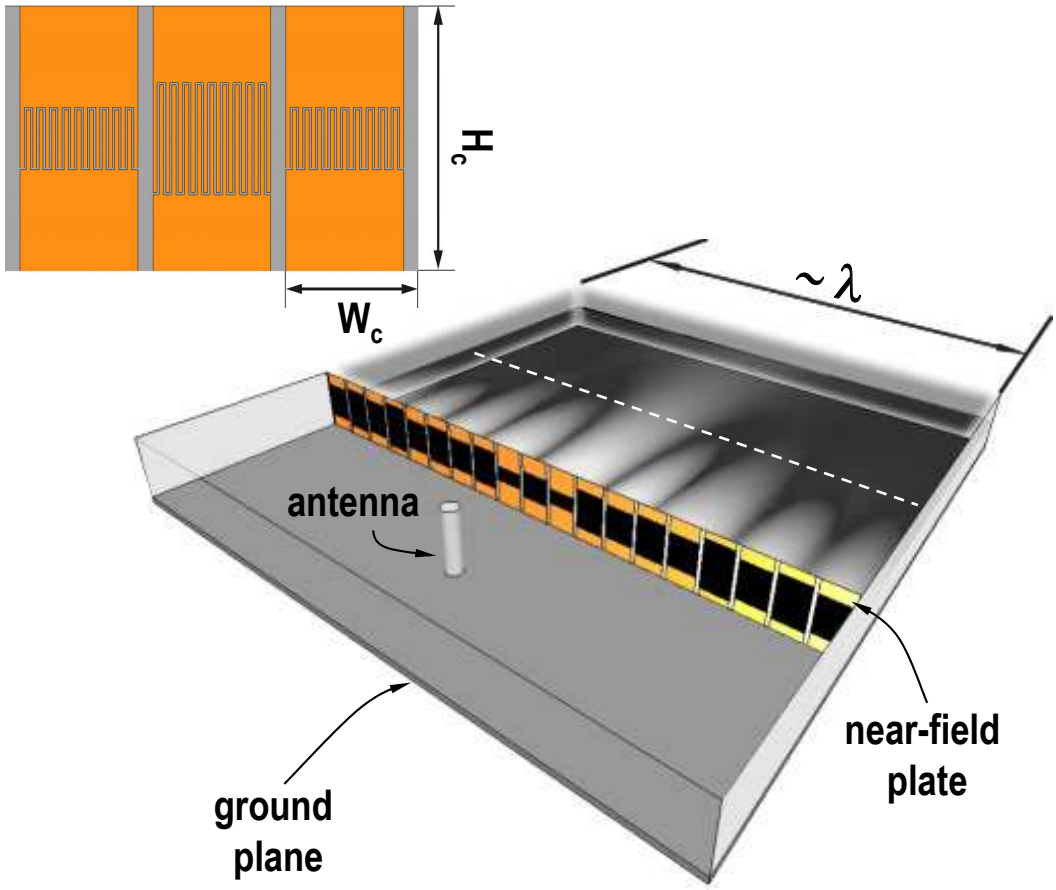

Figure 2.11: Schematic showing the experimental setup used to test the first experimental near-field plate reported in [14]. The figure shows the coaxially-fed dipole antenna (cylindrical source) and near-field plate inside a parallel plate waveguide. The top ground plane has been removed for clarity. The near-field plate consists of an array of interdigitated capacitors printed on an electrically-thin microwave substrate. Also shown is a contour plot of the simulated electric field on the image side (logarithmic scale). The dashed white line denotes the focal plane. The three central elements of the near-field plate are shown in the inset; $H_c = 15.0$ mm, $W_c = 7.5$ mm.

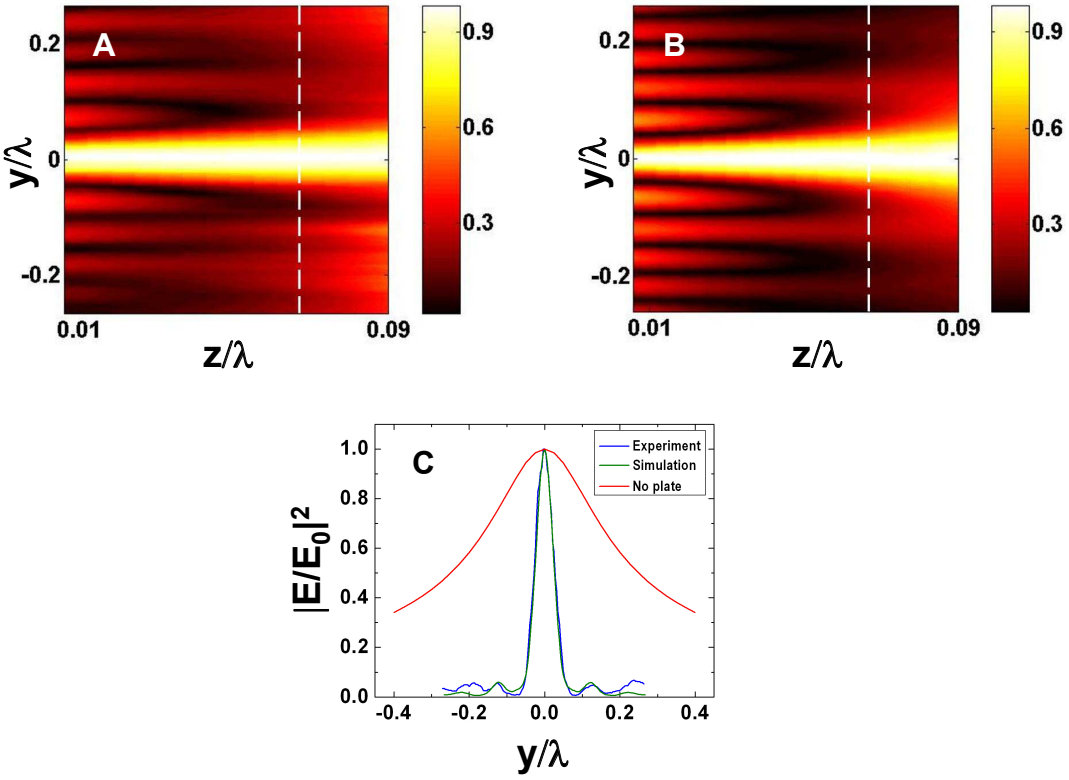

Figure 2.12: Normalized plots of the electric field (image side). Contour plot of the experimental (A) and simulated (B) electric field amplitude. The focal planes are denoted by the dashed white lines. (C) Normalized intensity along the focal plane of the near-field plate. The red curve shows the electric field due to the coaxially-fed antenna in the absence of the near-field plate (form [14]).

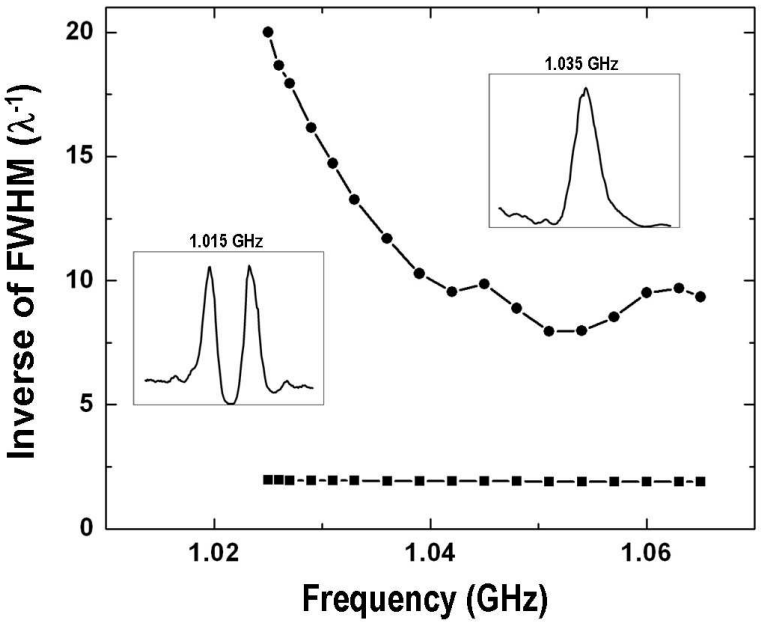

Figure 2.13: Resolution (FWHM of the focus) versus frequency for the near-field plate (circles). At frequencies above 1.025 GHz, the focal pattern exhibits a single peak (right inset) while, at frequencies below this value, there are multiple peaks (left inset). Also shown is the theoretical FWHM of the field intensity at the focal plane, when the near-field plate is not present (squares). The lines are a guide to the eye (form [14]).

3.0

A Linearly Corrugated Near-Field Plate

3.1 Introduction

In the previous chapter, the operation of near-field plates and the procedure used to design them were thoroughly examined using analytical and numerical approaches. The first experimental near-field plate, consisting of an array of interdigitated capacitors, was also presented. The near-field plate configuration presented in the previous chapter was excited by a cylindrical source and exhibited significant reflection. For many applications, it is more practical to excite the near-field plate through a waveguide. Waveguide excitation also allows for impedance matching to eliminate reflections. Therefore, our goal in this chapter is to design a near-field plate which can be fed through a waveguide.

The near-field plate presented in this chapter, referred to as linearly corrugated near-field plate, consists of a slit (parallel plate waveguide) surrounded with equally-spaced grooves with non-periodically varying depths, as shown in Figure 3.1. The grooves serve as parasitic elements which shape the radiation from the slit to form a prescribed subwavelength focus. The spacing, and the width of the grooves are uniform while the depth of the grooves is designed to shape the desired focal pattern. This non-periodically corrugated near-field plate should not be confused with periodically corrugated structures discussed in earlier works [32–43]. In these earlier works, periodic corrugations were used to beam radiation into the far field, in contrast to the non-periodically corrugated near-field plate presented here which tailors the near field. An overview of earlier works and their fundamental differences with corrugated near-field plates are presented in the next subsection.

In this chapter, it is demonstrated that a linearly corrugated near-field plate (shown in Figure 3.1) can focus electromagnetic field with subwavelength resolution. A procedure for designing the device to achieve a desired subwavelength focal pattern is outlined. Two different corrugated near-field plates are developed and their performance is studied in full-wave simulation. Close agreement between simulation and theory is demonstrated. In the first example, a corrugated near-field plate fed through a central slit in a metallic surface is considered. Full-wave simulation results confirming the plate's ability to form subwavelength focal patterns are reported. It is also demonstrated that the corrugated near-field plate is robust to practical losses and it can be impedance matched to its waveguide feed.

In the second example, a corrugated near-field plate with corrugations on both sides is considered. The two sides of the plate are connected by a central slit. One side features a periodic corrugation, which will be referred to as the input corrugation (IC), while the other side features a non-periodic corrugation, which will be referred to as output corrugation (OC). The periodic IC is illuminated by a plane-wave and it enhances the transmission of the incident plane wave through the central slit. The non-periodic OC, on

the other hand, focuses the wave transmitted through the slit to a subwavelength focus. Therefore, the overall function of this corrugated near-field plate is similar to that of a lens: the IC collects the incident plane-wave radiation, which is then transmitted through the central slit and focused to a subwavelength focus by the non-periodic OC. Finally, the corrugated near-field plate presented in the second example is fabricated and its measurement results are reported. Experimental results confirm that the linearly corrugated near-field plate produces a focal pattern significantly narrower than that formed by a single slit.

3.1.1 Periodic vs. Non-periodic Corrugation

Over the past few years, there has been growing interest in tailoring far field radiation using periodic corrugations or holes. Much of this interest was initiated by the discovery of extraordinary optical transmission through metallic films perforated with subwavelength holes [32–34]. This work prompted numerous theoretical and experimental studies on light propagation along periodic plasmonic surfaces. It also initiated the investigation of enhanced transmission and beaming through a single subwavelength hole/slit in a metal film surrounded by wavelength-scaled grooves [35–37]. Various geometries were considered including circular holes with concentric grooves and slits flanked by linear arrays of grooves. From an antenna perspective, the periodic grooves increase the antenna aperture - the area over which the electromagnetic wave is collected or radiated. This enhanced transmission/beaming through a single subwavelength hole was not only observed for periodically patterned plasmonic films, but also patterned conducting surfaces [38–41]. Much like a metallic film at optical frequencies that supports surface plasmons, the patterned conducting surface exhibits an inductive surface impedance that supports bound P-polarized surface waves (spoof surface plasmons) [42]. By periodically perturbing a plasmonic or conventional conducting metal film at a spacing close to guided wavelength, a leaky $n = -1$ spatial harmonic (diffracted beam) can be generated that delocalizes the radiation, in effect creating a leaky-wave antenna that has a directive far-field pattern [41].

The periodically structured surfaces described above enhance transmission and beam radiation into the far field. In contrast, corrugated near-field plates possess non-periodic grooves which provide extreme electromagnetic confinement. They manipulate the near field to create a subwavelength focal pattern at a near-field focal distance. It should be noted that, even in [43], where a non-periodic corrugation was considered, the device still operated in the far field and achieved diffraction-limited focusing.

3.2 Design Procedure

We will consider a symmetric linearly corrugated near-field plate with a finite number of $\pm N$ grooves on each side of the central slit, as shown in Figure 3.1. The grooves have uniform width w and spacing a, while their corresponding depths are non-periodically varied and denoted as d_{-N} to d_N. It is assumed that the grooves are infinite in the x direction and the metallic surface into which the grooves are placed is infinite in the x and y directions. In the design process, the corrugated near-field plate is first viewed as a waveguide-fed slit in a modulated, non-periodic impedance sheet, as shown in Figure 3.2. In the illustration, the contour plot at the exit face of the slit represents a possible impedance variation realized using non-periodic corrugations. The grooves and central slit (shown in Figure 3.1) are apertures within an infinite metallic surface, and therefore can be modeled as an array of magnetic currents over an infinite ground plane. The magnetic currents are equivalent sources with complex amplitudes equal to

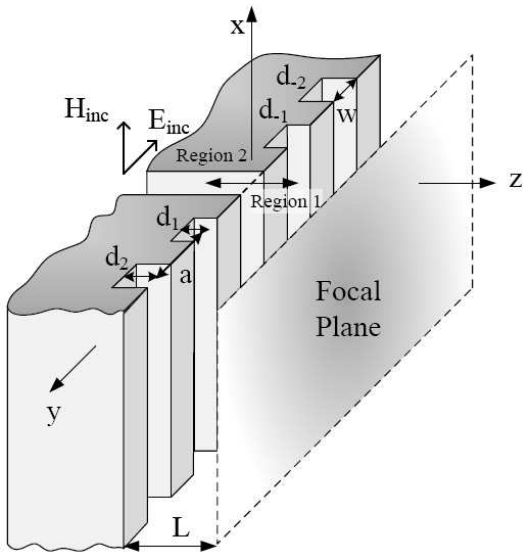

Figure 3.1: A linearly corrugated near-field plate consisting of a waveguide-fed slit in a non-periodically grooved metallic surface. The grooves have uniform width, w, and are equally spaced at a distance, a, from each other. The depth of each groove is non-periodically varied (form [16]).

the tangential electric field in the central slit and grooves [34, 44]. The depicted surface impedance simply represents the ratio of the magnetic current to the tangential magnetic field at $z = 0^+$.

The procedure for designing a corrugated near-field plate involves a few basic steps. The first step is to find the magnetic current density $M(y)\hat{x}$ on the plate needed to produce the desired focal pattern, in the presence of the excitation (the waveguide-fed slit). The second step involves computing the magnetic field at the surface of the plate, $H_{total} = H(y, z = 0^+)\hat{x}$, resulting from the magnetic current density and excitation. The third step is to calculate the surface impedance required to produce the focal pattern. The surface impedance is calculated by taking the ratio of $M(y)$ to H$(y, z = 0^+)$. The final step is to optimize the depth of the grooves surrounding the central slit, in order to realize this surface impedance profile.

The magnetic current density on the plate needed to produce the desired focal pattern $H_{focal}(y) = H(y, z = L)$ can be found by solving an integral equation that relates the incident magnetic field H_{inc}, $M(y)$, and $H_{focal}(y)$. The electromagnetic boundary value problem can be divided into two regions: region 1 is the unbounded space $z > 0$, and region 2 is the region within the waveguide feed. Using the aperture formulation for TM scattering [44], equivalent electromagnetic problems for the two regions can be written, that are connected through the continuity of tangential magnetic and electric field through the central slit. The equivalent problem for region 1 involves a magnetic current density $2M(y)$ radiating in free space to produce the desired focal pattern $H_{focal}(y)$, and is governed by the following integral equation,

$$\frac{-\omega\epsilon_0}{2\pi}\int_{-W/2}^{W/2} M(y')H_0^{(2)}(k\sqrt{(y-y')^2+L^2})dy' = H_{focal}(y) \tag{3.1}$$

where W is the total width of the corrugated near-field plate, and $H_0^{(2)}$ is the zeroth order Hankel function of the second kind. Given the desired focal pattern H_{focal}, Equation (3.1) can be solved using the Method of Moments [44]. The magnetic current density is treated as the unknown and discretized into $2N + 1$ elements with Δy width. For example, pulse basis functions and the point matching method can be used

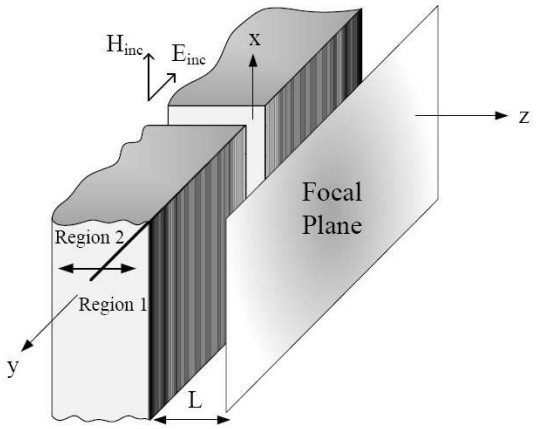

Figure 3.2: A simplified model of the corrugated near-field plate shown in Figure 3.1. The model consists of a waveguide-fed slit in a non-periodic impedance sheet (form [16]).

to convert Equation (3.1) into the following matrix equation:

$$\frac{-\omega\epsilon_0}{2\pi}\sum_{m=-N}^{N} M_m H_0^{(2)}(k\sqrt{(|n-m|\Delta y)^2+L^2})w = H_{focal,n} \tag{3.2}$$

where n is an integer from $-N$ to N, w is the width of the grooves, $M_m = M(y = m\Delta y)$ and $H_{focal,n} = H_{focal}(n\Delta y)$. Since the magnetic current density has a non-zero value only at the grooves locations, the width of each element is represented by w in Equation (3.2). It should also be noted that M_0 represents the magnetic current assigned to the central slit. The equivalent problem for region 2 involves an incident TEM wave on a magnetic current density, M_0. Considering only the dominant TEM mode within the waveguide, the electromagnetic fields in region 2 ($z < 0$) are governed by the following equation,

$$2H_{inc} + \frac{M_0}{\eta} = H_{total,n=0} \tag{3.3}$$

where $H_{total,n} = H_{total}(z = 0, y = n\Delta y)$, H_{inc} is the magnetic field of the incident electromagnetic wave, and η is the characteristic impedance of free space. The magnetic current density M_0, that is common to Equations (3.2) and (3.3), ensures the continuity of the tangential electric field through the central slit. The continuity of the magnetic field is enforced by ensuring that the magnetic field $H_{total}(n\Delta y = 0)$ at the central slit,

$$H_{total,n} = \frac{-\omega\epsilon_0}{2\pi}\sum_{m=-N}^{N} M_m H_0^{(2)}(k|(n-m)\Delta y|)w \tag{3.4}$$

produced by the magnetic currents M_m in Equation (3.2), is the same as the one which appears in Equation (3.3).

By solving Equation (3.2), the magnetic current densities needed to produce the focal pattern H_{focal} can be found. Given the magnetic current densities and Equation (3.4), the required incident magnetic field H_{inc} can be computed using Equation (3.3). From the magnetic current densities and $H_{total,n}$, the surface impedance depicted in Figure 3.2 can be found. The surface impedance is then simply:

$$Z(y = n\Delta y) = Z_n = \frac{M_n}{H_{total,n}} \tag{3.5}$$

In the final step of the design process, the surface surrounding the slit is corrugated (see Figure 3.1) in order to realize the impedance profile given by Equation (3.5). Only the imaginary part of the impedance is used given that the real part is negligible [12]. The width, w, and spacing, a, of all of the grooves are kept the same, while the depth, d_n, of the grooves is varied. Each groove can be considered as a short-circuited waveguide. By varying the depth d_n of each groove, its input reactance can be changed. Using this short-circuited waveguide model, the input impedance of each groove is $j\eta \tan kd_n$ [34, 45]. This expression for the input impedance pertains to the idealized case where there are no fringing fields, and only the dominant TEM mode is present within the waveguide. To accurately determine the depth of the grooves, a full-wave electromagnetic solver can be used that takes into account all parasitics and higher order waveguide modes that are excited.

3.3 Simulation Results

To demonstrate the utility of the design procedure, we present two different corrugated near-field plates. Both plates are designed following the procedure outlined above and full-wave simulation results verifying their operation are presented. Later in this chapter, the experimental results verifying the performance of the second example are presented.

3.3.1 Example 1

In the first example, a linearly corrugated near-field plate with the following parameters: $L = \frac{\lambda}{15}, a = \frac{\lambda}{40}, w = \frac{\lambda}{80}, N = 19$ is considered. The magnetic-field focal pattern is assumed to be a sinc function with a null-to-null beamwidth of $\lambda/10$,

$$H_{focal}(y) = \frac{\sin(qy)}{qy} = \mathrm{sinc}(qy) \tag{3.6}$$

where $q = 10k$ determines the null-to-null beamwidth. The wavelength of operation is set to 30 cm, corresponding to frequency of 1 GHz. At first, we assume that the metal is a lossless perfect electric conductor (PEC). Following the design procedure above, the required magnetic current densities were found and are listed in Table 3.1. The magnetic currents listed in Table 3.1 are normalized to the incident electric field, found using Equation (3.3). Table 3.1 shows that the phase of adjacent magnetic current densities is reversed. As pointed out in the previous chapter, this rapid phase variation is a characteristic feature of the near-field plates. Given the magnetic current densities, Equation (3.5) is used to obtain the required surface impedance. Neglecting the real part of the surface impedance, the depths of the grooves needed to produce the focal pattern were found. The computed depths are shown in Figure 3.3.

The focal pattern produced by this corrugated near-field plate is plotted in Figure 3.4. The plot also shows the ideal focal pattern given by Equation (3.6) (*Theory*), as well as the focal pattern produced by the discretized magnetic currents M_m (given by Equation (3.2)) found using the Method of Moments (*MoM*). The near-field plate is simulated using a commercial finite element electromagnetic solver Comsol Multiphysics (*COMSOL*). The three focal patterns are nearly identical, thereby validating the described design procedure. It should be noted, however, that there was a slight frequency shift in the designed corrugated near-field plate. The *COMSOL* pattern is plotted at 1.0015 GHz, while the other two curves are at 1.0 GHz. This slight frequency shift in center frequency can be attributed to numerical inaccuracies and the initial assumption that the electric field is constant across the grooves.

Groove Index (n)	Normalized Magnetic Current Densities(M_n/E_{inc})
0	$1.9963\angle 176.4247°$
1	$0.4975\angle 176.5339°$
2	$1.5722\angle -3.6577°$
3	$1.0262\angle -3.6804°$
4	$0.8870\angle 176.4664°$
5	$0.9757\angle 176.4556°$
6	$0.5099\angle -3.7405°$
7	$0.8217\angle -3.6830°$
8	$0.3109\angle 176.5874°$
9	$0.6968\angle 176.4547°$
10	$0.2251\angle -3.8885°$
11	$0.5676\angle -3.6546°$
12	$0.1173\angle 177.0418°$
13	$0.5674\angle 176.3452°$
14	$0.2117\angle -4.2414°$
15	$0.2830\angle -3.1021°$
16	$0.1836\angle -5.2499°$
17	$0.8258\angle 175.8882°$
18	$0.6505\angle -4.4743°$
19	$0.1660\angle 173.9888°$

Table 3.1: The magnetic current densities representing the grooves of the designed near-field plate. The magnetic current densities are normalized to the incident electric field computed using Equation (3.3).

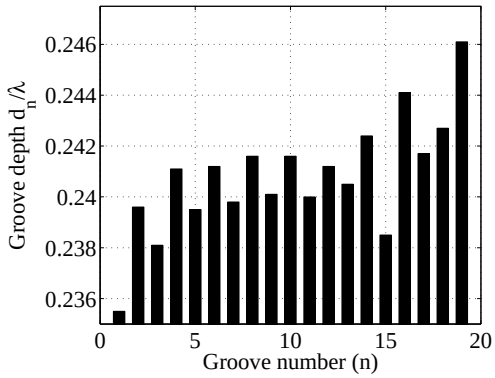

Figure 3.3: The groove depths for the corrugated near-field plate shown in Figure 3.1, designed to operate at 1.0 GHz. The plot is symmetric: $d_n = d_{-n}$ (form [16]).

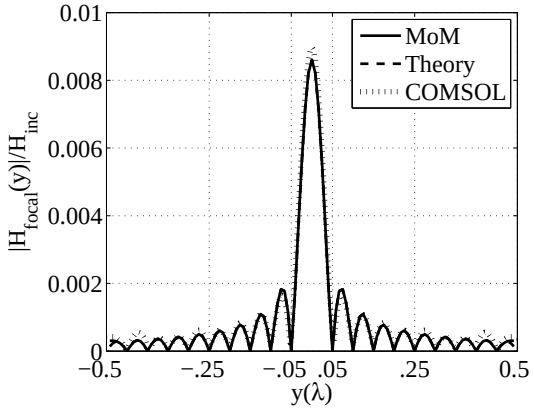

Figure 3.4: Focal patterns at 1.0 GHz formed by the near-field plate depicted in Figure 3.1. The curve labeled *MoM* represents the focal pattern produced by M_m given by Equation (3.2), *Theory* is a plot of Equation (3.6), and *COMSOL* is the focal pattern produced by the designed corrugated near-field plate (form [16]).

Moreover, the effect of practical losses on the performance of the corrugated near-field plate is studied using Comsol Multiphysics by replacing the PEC boundaries of the structure with copper. A contour plot of the magnetic field is shown in Figure 3.5 for a plate with copper boundaries. The focal patterns with losses (copper) and without losses (PEC) are compared in Figure 3.6. As can be seen, only slight changes in the pattern result from the losses.

Although the designed corrugated near-field plate maintains a subwavelength focus despite losses, it still suffers from an impedance mismatch at its input, which limits the device's power transfer capability. To remedy this, the corrugated surface was impedance matched to its waveguide feed using a single-stub matching network [45], as shown in Figure 3.5. The stub is located at 0.49571λ from the opening of central slit and has a length of 0.24017λ. The stub was chosen to have a width equal to that of the central slit. Using the stub matching network, a return loss of around -15 dB was obtained for the plate. Through impedance matching, the maximum amplitude of the focal pattern ($H_{focal,0}$) was increased from $0.0098H_{inc}$ to $0.0817H_{inc}$. Therefore, impedance matching can clearly improve power transfer.

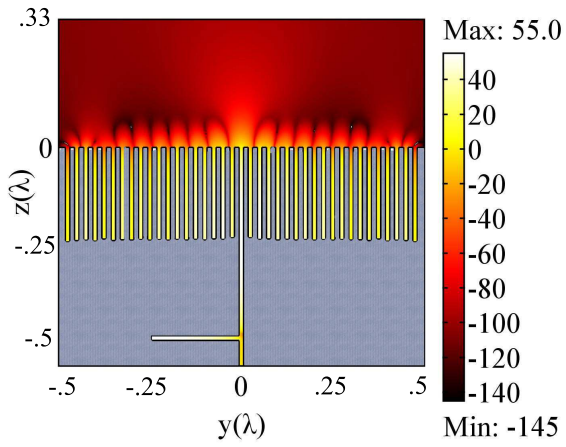

Figure 3.5: A cross-sectional view of the corrugated near-field plate designed to operate at 1.000 GHz. A contour plot (in dB) of the x-directed magnetic field formed by the device is shown, given a TEM wave with magnetic field $H_{inc} = 1$ incident from the waveguide feed. The magnetic field contour plot includes the effect of losses. The stub attached to the waveguide feed is used to impedance match the device (form [16]).

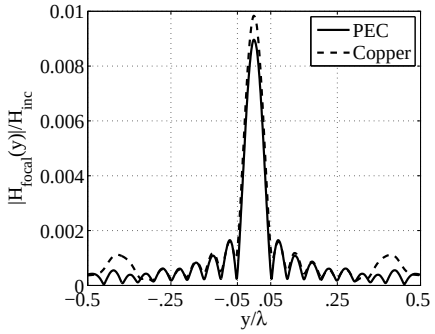

Figure 3.6: The focal pattern produced by the corrugated near-field plate with PEC (lossless) boundaries (solid line) and with copper (lossy) boundaries (dashed line), computed using Comsol Multiphysics (form [16]).

3.3.2 Example 2

The linearly corrugated near-field plate presented in the previous example was fed through its central slit by a waveguide. The linearly corrugated near-field plate presented here is slightly modified. The modified structure presented in this example is shown in Figure 3.7 and consists of two identical metallic slabs placed closely together. The gap between the slabs serves as the central slit. Both sides of each slab feature corrugations which run along the length of the slab (see Figure 3.7). The slabs are illuminated from one side by a plane wave, which is partly transmitted through the central slit. The side of the plate illuminated by the plane wave, features a periodic input corrugation, referred to as IC. The other side of the plate features a non-periodic output corrugation, referred to as OC. The periodic IC is similar to the periodic corrugations discussed in subsection 3.1.1. Their design and operation have been thoroughly discussed in literature [32–43]. The purpose of the IC is to enhance transmission of the plane wave energy through the central slit. On the other hand, the non-periodic OC, which forms the subwavelength

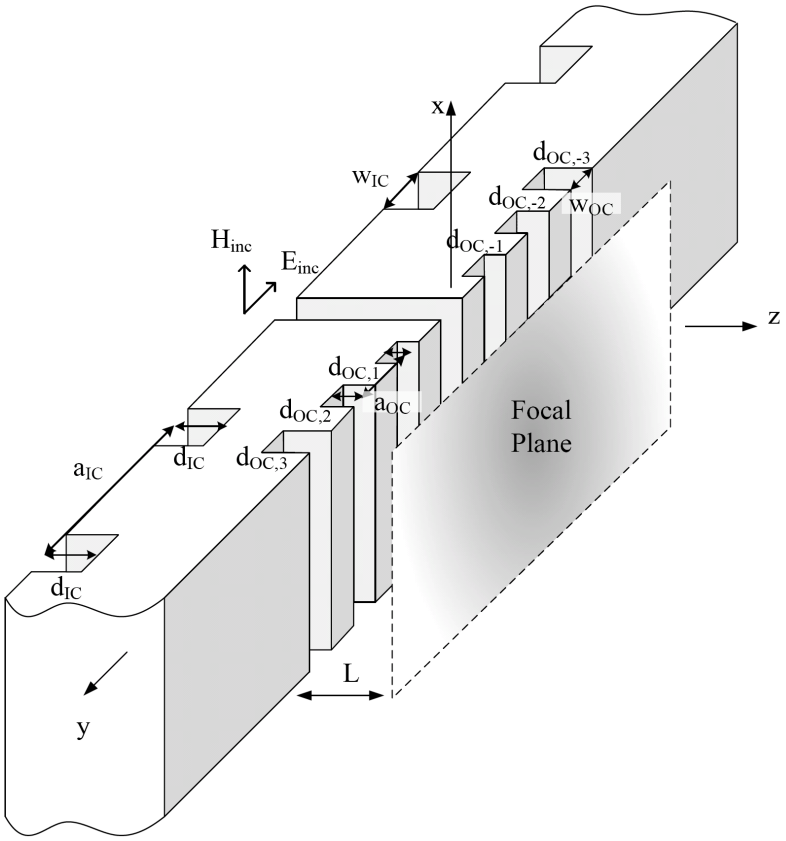

Figure 3.7: The linearly corrugated near-field plate discussed in section 3.3.2 (example 2). The plate consists of two identical metallic slabs, placed closely together, to form the central slit. One side is periodically corrugated and is referred to as input corrugation (IC). The other side is non-periodically corrugated and referred to as output corrugation (OC). The IC enhances the transmission through the central slit while the OC forms a subwavelength focus on the other side.

focus, is in fact a realization of the corrugated near-field plate presented in Example 1. Since the roles and operation of IC and OC are independent of each other, they can be designed separately. The OC is designed following the procedure outlined in Example 1 and its performance is studied through full-wave simulation. The IC is designed following an established procedure [32–43]. At the end, the performance of the entire structure including both IC and OC is studied using full-wave simulation. This structure is examined through experiment in the next section.

In the design process, the slabs are initially assumed to be infinitely wide. Subsequently, the effects of finite width and edge diffraction are considered. The first step in the design procedure of the output corrugation is to choose the desired focal pattern. In the previous example, a sinc function magnetic-field focal pattern with null-to-null beamwidth of $\lambda/10$ was chosen (see Figure 3.8 (a)). This choice results in a transverse electric-field (E_y) focal pattern with null-to-null beamwidth of $\lambda/15$ as shown in Figure 3.8 (b). Figure 3.8 (b) reveals that the transverse electric-field (E_y) focal pattern exhibits significantly large side lobes. To remedy this, the magnetic-field focal pattern was chosen to be a zeroth-order Hankel function of the second kind (see Figure 3.8 (c)), with its spatial spectrum truncated to $q = 15k$. The corresponding E_y focal pattern approximates a sinc function with null-to-null beamwidth of $\lambda/15$ with

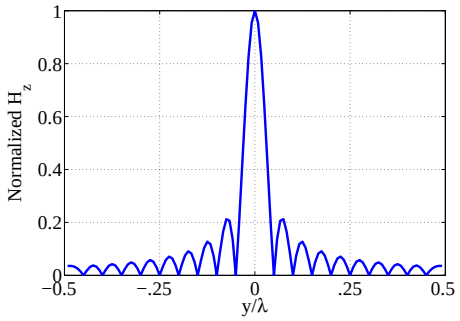

(a) Example 1 magnetic-field focal pattern

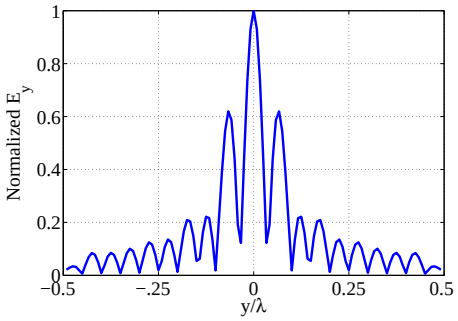

(b) Example 1 transverse electric-field focal pattern

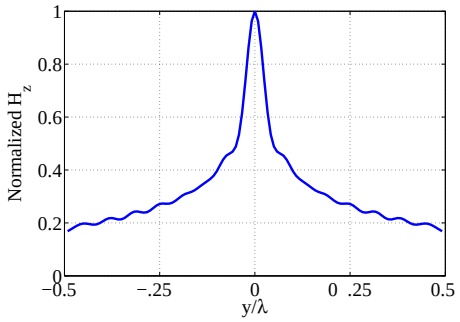

(c) Example 2 magnetic-field focal pattern

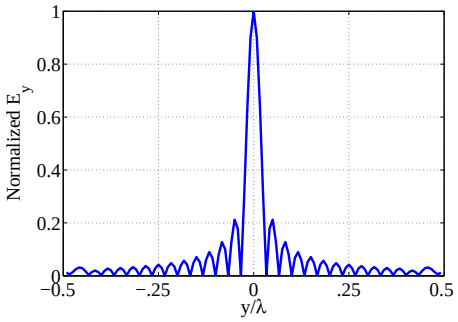

(d) Example 2 transverse electric-field focal pattern

Figure 3.8: Comparison of the desired focal patterns in example 1 and example 2. (a) Example 1 magnetic-field focal pattern: a sinc function with null-to-null beamwidth of $\lambda/10$. (b) Example 1 transverse electric-field focal pattern. (c) Example 2 magnetic-field focal pattern: a zeroth order Hankel function of the second kind with its spatial spectrum truncated to $q = 15k$. (d) Example 2 transverse electric-field focal pattern which approximates a sinc function with null-to-null beamwidth of $\lambda/15$.

small sidelobes, as shown in Figure 3.8 (d).

The operating frequency is set to 10.0 GHz, corresponding to $\lambda = 3.0$ cm. The other parameters are the same as those in the previous example: $L = \frac{\lambda}{15}, a_{OC} = \frac{\lambda}{40}, w_{OC} = \frac{\lambda}{80}, N_{OC} = 19$. Given these parameters and assuming lossless conditions, the required OC's groove depth variation, $d_{OC,n}$, was obtained and shown in Figure 3.9. Using this groove depth variation, the structure was simulated using Comsol Multiphysics and the resulting focal patterns are plotted in Figure 3.10 and denoted as *COMSOL*. For comparison, the ideal focal patterns shown in Figure 3.8 are also plotted and labeled as *Theory*. In addition, the focal patterns computed using the Method of Moments are shown and denoted as *MoM*. To compute the *MoM* plot, the focal pattern produced by the magnetic current density on the OC is found. The induced magnetic current densities are found by substituting the imaginary part of the required surface impedance, Z_n, into the equation below:

$$\frac{M_n}{Z_n} = \frac{\omega\epsilon_0}{2\pi} \sum_{m=-N}^{N} M_m H_0^{(2)}(k|(n-m)\Delta y|)w \tag{3.7}$$

Figure 3.10 shows good agreement between *MoM* and *Comsol*, and thereby verifies the design procedure.

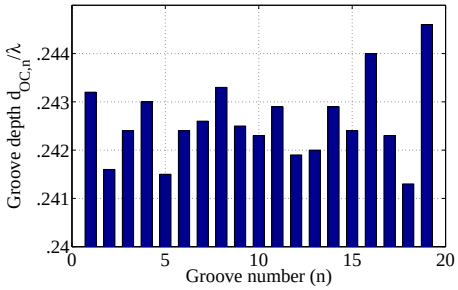

Figure 3.9: The groove depths for the OC of the near-field plate shown in Figure 3.7. The plate is designed to operate at 10.0 GHz. The near-field plate is symmetric: $d_{OC,n} = d_{OC,-n}$ (form [17]).

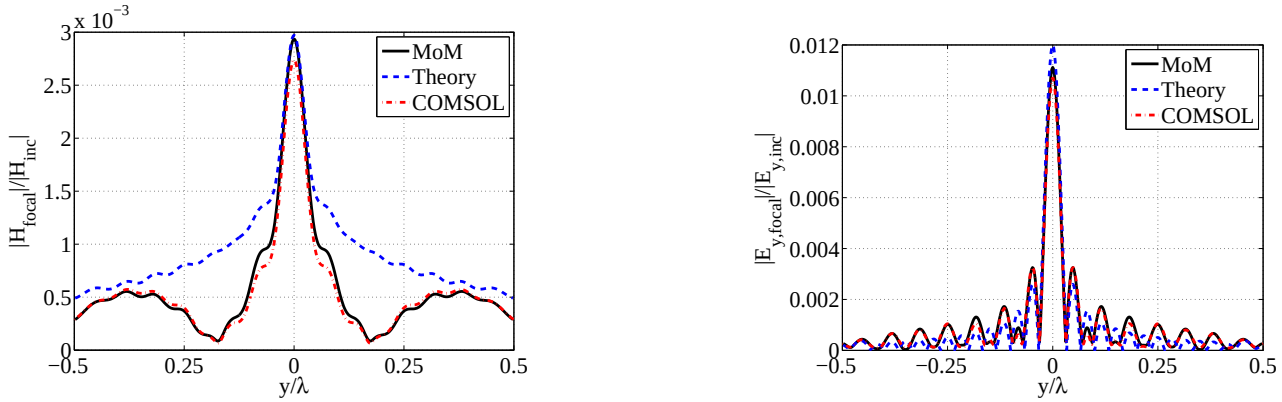

(a) Normalized magnetic-field focal pattern

(b) Normalized transverse electric-field focal pattern

Figure 3.10: Normalized (a) magnetic-field and (b) transverse electric-field focal patterns produced by the OC of the near-field plate shown in Figure 3.7. The curve labeled *Theory* is the plot of the theoretical focal pattern. The curve *MoM* represents the focal pattern produced by the magnetic current densities computed using Equation (3.7), and *COMSOL* is the focal pattern produced by the designed corrugated near-field plate.

However, both *MoM* and *Comsol* show slight differences from the ideal pattern. This difference is due to the fact that the real part of the required impedance profile is ignored in the design procedure, when in fact it is not negligible in this particular case. One should note that the real part of impedance profile cannot be realized by varying the grooves' depths. Finally, it should be emphasized that the simulation results are presented at 10.006 GHz, which differs from the design frequency of 10.0 GHz by 0.6%. As before, this slight frequency shift is attributed to numerical inaccuracies and the initial assumption that the electric field is constant across the grooves.

In order to study the effect of practical losses on the performance of the plate, the designed OC was resimulated with the PEC boundaries replaced with copper boundaries. The focal pattern produced by the lossy near-field plate is depicted in Figure 3.11 and denoted as *Copper*. The pattern produced by the lossless near-field plate is also depicted and denoted as *PEC*. The effect of loss is more pronounced here than in the previous example (see Figure 3.6) since conductor losses are higher due to the ten fold increase in frequency [45].

In the next step, the IC is designed to maximize the transmission through the central slit. The IC design procedure has been outlined previously in literature [32–43]. Following the established procedure,

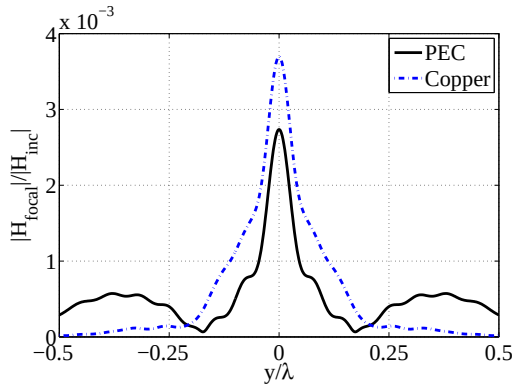

(a) Normalized magnetic-field focal pattern

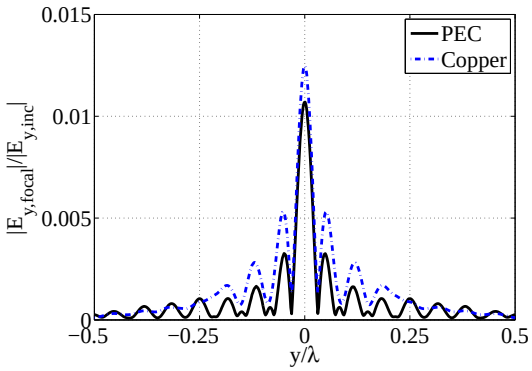

(b) Normalized transverse electric-field focal pattern

Figure 3.11: Normalized (a) magnetic-field and (b) transverse electric-field focal patterns produced by the OC of the corrugated near-field plate shown in Figure 3.7 with PEC boundaries (solid line) and with copper boundaries (dashed line). The patterns are computed using Comsol Multiphysics.

the IC was designed and its parameters are as follows: $N_{IC} = 5$, $a_{IC} = 27.6 \text{ mm} = 0.92\lambda$, $w_{IC} = 2.76 \text{ mm} = 0.092\lambda$, and $d_{IC} = 4.15 \text{ mm} = 0.138\lambda$. It is worth noting that the input corrugation is periodic with the groove separation a_{IC} equal to a guided wavelength of the surface mode supported by the IC at 10.0 GHz. Also, the depth and width of the input corrugations are subwavelength. Finally, the thickness of the slab is chosen to be $H = 14$ mm, which corresponds to a resonant length ($\lambda/2$). This choice further enhances transmission through the central slit.

Given the parameters above for IC and OC, the corrugated near-field plate shown in Figure 3.7 was simulated in Comsol Multiphysics. Conductor losses were included in the simulation and the results are shown in Figure 3.12, and denoted as *IC+OC Lossy*. For comparison purposes, the focal patterns produced by the plate when the OC is removed are also depicted and denoted as *IC Lossy*. The focal patterns produced by the plate with the OC are significantly narrower than those produced without the OC.

In order to illustrate the effect of losses and diffraction from the edges separately, the focal patterns produced for different cases are depicted in Figure 3.13. The first graph is the same pattern shown in Figure 3.12 and is labeled as *IC+OC Lossy*. The second graph, labeled as *IC+OC Lossless*, is the pattern produced by the structure when there is no loss. As noted earlier, the effect of conductor loss is noticeable due to the high frequency of operation. The third graph, labeled as *OC Lossy*, is the focal pattern produced by the lossy structure when the IC is removed. When the IC is removed, the diffraction from the edges significantly changes the focal pattern. The last graph is labeled *OC Lossless*. This graph is the focal pattern produced by a lossless plate with the IC removed. These focal patterns significantly differ from the ones plotted in Figure 3.10. This difference clearly demonstrates the effects of the edge diffraction.

In the next section, the corrugated near-field plate presented in this example is fabricated and tested. The setup used to measure the plate's focal patterns is described in detail. Magnetic field measurements for the fabricated structure are also reported. For comparison, the patterns produced by a single slit are also measured. It is shown that the corrugated near-field plate produces significantly narrower patterns than a single slit in a metallic plate of equal dimensions with the same IC.

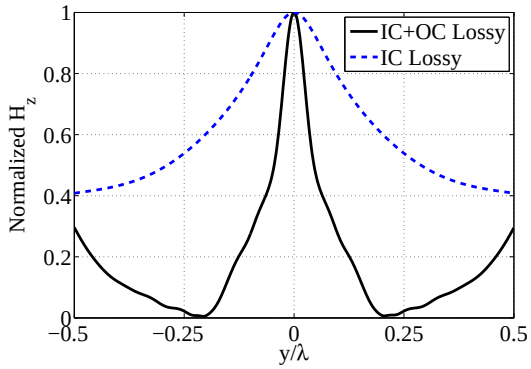

(a) Normalized magnetic-field focal pattern

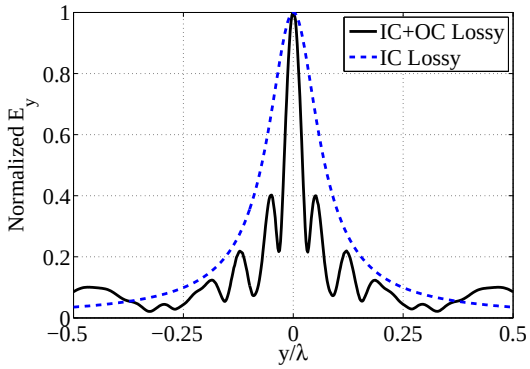

(b) Normalized transverse electric-field focal pattern

Figure 3.12: Normalized (a) magnetic-field and (b) transverse electric-field focal patterns produced by the corrugated near-field plate shown in Figure 3.7. The *IC+OC Lossy* plot represents the patterns produced by the lossy near-field plate while the *IC Lossy* plot represents the patterns produced by the lossy plate with the output corrugation (OC) removed.

3.4 Measurements

The experimental near-field plate consisted of two corrugated copper plates fabricated with 25 micron accuracy using wire electrical discharge machining (EDM). The corrugated near-field plate was measured using the setup shown in Figure 3.14. In this setup, a Gaussian beam telescope system [46, 47] was used to illuminate the IC of the corrugated plate. The magnetic field of the Gaussian beam was oriented along the grooves. The Gaussian beam telescope was connected to port 1 of a network analyzer. To detect the magnetic-field focal pattern produced by the plate, a shielded loop antenna was scanned along the y direction at a distance 1 mm from the OC. The shielded loop had a diameter of 4.5 mm, and was made from 0.047 inch semi-rigid coaxial cable. The loop was connected to port 2 of the network analyzer. In this setup, the S_{21} measured by the network analyzer is a measure of the transmitted magnetic field.

The measured magnetic-field focal pattern is shown in Figure 3.15, and is denoted as *Corrugated Measurement*. To emphasize the narrowness of the focal pattern produced by the OC, we have also plotted a curve showing the measured magnetic-field pattern when the OC was removed (covered by copper tape), and is denoted as *Slit Measurement*. By covering the OC with copper tape, the grooves were short circuited and effectively removed. Therefore, the plate with the OC covered acted like a single slit with enhanced transmission resulting from the IC. The *Corrugated Measurement* exhibits a FWHM of $\lambda/9.23$ which is 3 times narrower than the *Slit Measurement* plot that exhibits a FWHM of $\lambda/3.07$. It should be noted that the simulated focal pattern, denoted as *Corrugated Simulation*, is slightly narrower than the measured one, exhibiting a FWHM of $\lambda/11$. The increased width of the experimental focal pattern can be attributed to the size of the shielded-loop used to probe the magnetic field. The radius of the probe was larger than the groove spacing of the OC, which determines the resolution of the subwavelength focus. Therefore, the size of the shielded-loop limited the spatial resolution that could be detected. Finally, the measurement results are reported at 10.007 GHz, while the simulation results are reported at 10.006 GHz. This negligible frequency shift can be attributed to the 25 micron tolerance of the fabrication process.

In order to investigate the transmission enhancement achieved by the IC, the measured signal levels

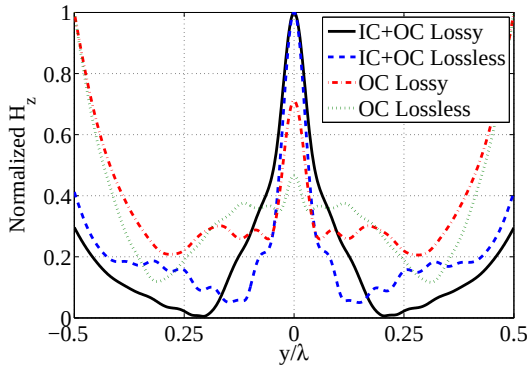

(a) Normalized magnetic-field focal pattern

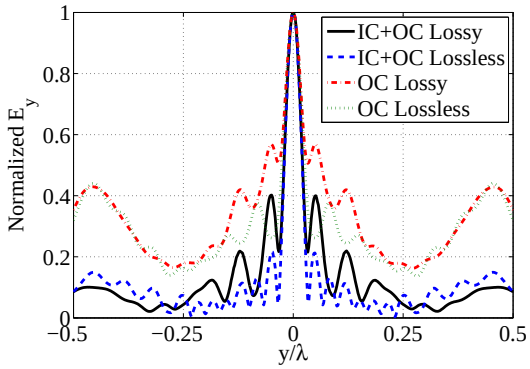

(b) Normalized electric-field focal pattern

Figure 3.13: Normalized (a) magnetic-field and (b) transverse electric-field focal patterns produced by the corrugated near-field plate shown in Figure 3.7. The *IC+OC Lossy* plot represents the pattern produced by the lossy plate. The *IC+OC Lossless* plot represents the pattern produced by the lossless plate. The *OC Lossy* plot represents the pattern produced by the lossy structure with the IC removed. The *OC Lossless* plot represents the pattern produced by the lossless plate with the IC removed.

detected by the loop placed close to the central slit are listed in Table 3.2. The signal levels when the IC is removed (covered by coper tape) are significantly lower than when the IC is present (not covered). These comparisons verify the enhanced transmission through the central slit achieved by the IC.

Measurement	S_{11} (dB)	S_{21} (dB)
IC+OC	-9.7	-33.8
OC	-3.7	-37.12
IC	-7.5	-28.2
single slit	-3.34	-33.3

Table 3.2: The transmitted magnetic field amplitude for the different input/output corrugation configurations. The magnetic field amplitude is measured by placing the shielded loop close to the central slit. The S_{11} and S_{21} values are signals measured by the network analyzer when port 1 is connected to the Gaussian beam telescope and port 2 is connected to the shielded loop. *IC+OC* represents the measured signal when both the input and output corrugations are present. *OC* represents the measured signal when the input corrugation is removed (covered by copper tape). *IC* represents the measured signal when the output corrugation is removed (covered by copper tape). *Single slit* represents the measured signal when both input and output corrugation are removed (covered by copper tape).

Finally, the emitted beam from the corrugated near-field plate with and without OC (single slit with IC) are compared in Figure 3.16. In the plot, the measured magnetic field (H_z) along each $z = z'$ plane has been normalized to its corresponding maximum value: $H_z(y, z = z')/H_z(y = 0, z = z')$. Figure 3.16 (a) shows the beam radiated from the near-field plate with the OC covered by copper tape while Figure 3.16 (b) shows the beam radiated from the near-field plate. These two figures confirm the near-field plate's superior ability to confine the electromagnetic near field over an extended operating distance.

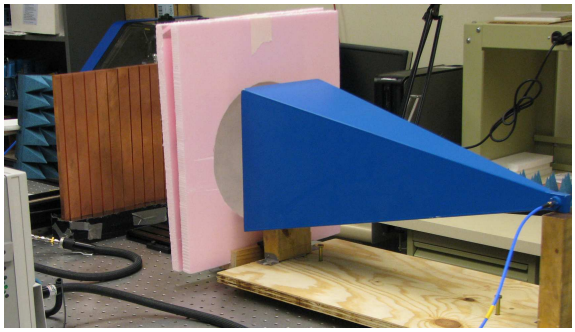

(a) Gaussian beam telescope illuminating IC

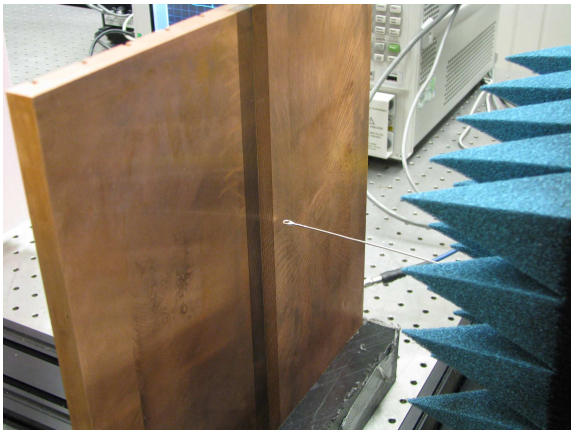

(b) Small loop measuring the pattern created by OC

Figure 3.14: Fabricated corrugated near-field plate and measurement setup. (a) The Gaussian beam telescope used to illuminate the input corrugation (IC). (b) The photograph depicts the small shielded loop used to measure the magnetic-field pattern created by the output corrugation (OC) (form [17]).

3.5 Conclusion

We have shown that a linearly corrugated near-field plate consisting of a waveguide-fed slit surrounded by non-periodic corrugations can focus electromagnetic fields to subwavelength resolutions. A general procedure for designing such a device was outlined. Two different examples of corrugated near-field plates were designed and studied in full-wave simulation. The effect of losses was also considered, and two different methods to improve the reflection from a near-field plate were demonstrated. In the first example, a single stub was used to reduce the reflections while in the second example, periodic input corrugations were used to reduce reflections and enhance transmission. Furthermore, an experimental corrugated near-field plate consisting of a single slit in a corrugated metallic plate was studied. The input face of the experimental plate was periodically corrugated to enhance transmission through the slit, while the output face of the plate featured a non-periodic corrugation which formed the subwavelength focus. Simulation and free-space measurements were reported at approximately 10 GHz, confirming the corrugated plate's ability to form a subwavelength focus with FWHM of $\lambda/9.23$ at a distance $\lambda/15$ from the output face of the plate. This study opens new opportunities to develop corrugated near-field plates at optical wavelengths using nanostructured metals such as silver and gold.

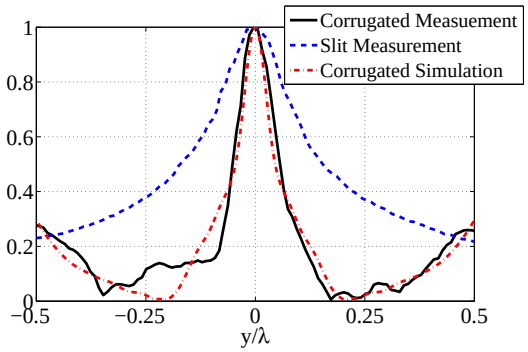

Figure 3.15: Normalized magnetic-field near-field patterns detected using the measurement setup shown in Figure 3.14. The *Corrugated Measurement* plot represents the measured magnetic-field pattern produced by the corrugated near-field plate while the *Slit Measurement* plot represents the pattern formed by the plate when OC is removed (covered by copper tape). The *Corrugated Simulation* plot is the simulated magnetic-field focal pattern produced by the near-field plate (computed using Comsol Multiphysics).

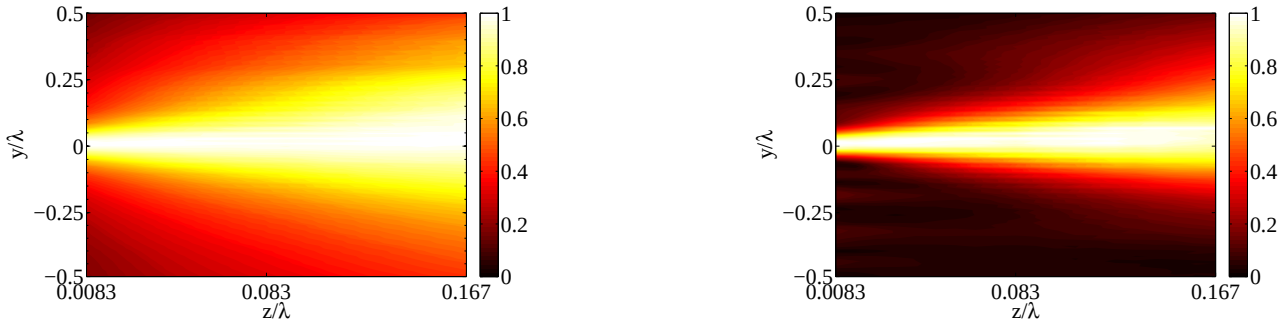

(a) Slit with IC

(b) Near-field plate

Figure 3.16: Measured beam emitted from (a) the corrugated near-field plate with OC removed (covered by copper tape) and (b) the corrugated near-field plate. In both plots, the measured field along each $z = z'$ plane is normalized to its maximum value: $H_z(y, z = z')/H_z(y = 0, z = z')$.

4.0

A Concentrically Corrugated Near-Field Plate

4.1 Introduction

In the previous chapter, a linearly corrugated near-field plate consisting of a waveguide-fed slit surrounded by linear, non-periodic corrugations was studied. It was shown that non-periodic corrugations can form a magnetic-field focal pattern (line focus) at approximately 1 GHz with a null-to-null beamwidth of $\lambda/10$ at a $\lambda/15$ focal length. The simulation results were then verified using an experimental corrugated near-field plate.

The results presented in the previous chapter proved that the linearly corrugated near-field plates can create subwavelength focal patterns. However, the linearly corrugated near-field plate still required further development to be of use in applications such as near-field probing. Specifically, the near-field plate presented in the previous chapter could only produce a 1-D subwavelength focus (line focus) while a 2-D subwavelength focus is needed in such an application. Also, the plate in previous chapter was excited using a parallel plate waveguide (slit) which may be difficult to feed or impedance match in practice. Therefore, our goal in this chapter is to design a near-field plate which forms a 2-D focus, and can be fed through a simple coaxial connector. Such a device can find many applications ranging from near-field probing and sensing systems to biomedical and data storage devices.

The near-field plate presented in this chapter consists of a coaxially-fed central aperture surrounded by periodically-spaced, concentric grooves. The grooves are spaced uniformly at a subwavelength distance and the depths of the grooves are non-periodically varied. The device considered is depicted in Figure 4.1, and will be referred to as a concentrically corrugated near-field plate. We will show that such a device can localize the electromagnetic field emitted by the central aperture to a 2-D subwavelength spot at a near-field distance (focal length) $z = L$. The near-field focal spot can be designed to be much smaller than that would be obtained by the central aperture alone. Therefore, this coaxially-fed concentrically corrugated near-field plate can provide extreme 2-D electromagnetic field confinement, and is well suited for applications such as a near-field probing.

This chapter is organized into five sections. At first, we outline a procedure for designing a concentrically corrugated near-field plate. Simulation results are presented which confirm the designed near-field plate's ability to form a 2-D subwavelength focus. Next, the performance of the concentrically corrugated near-field plate is studied in experiment. The electric-field patterns produced by the impedance matched, concentrically corrugated near-field plate are measured at various distances. It is experimentally verified that the near-field plate produces focal patterns with significantly narrower beamwidths compared to those produced by a coaxial probe of the same dimensions. The measured electric-field patterns are also

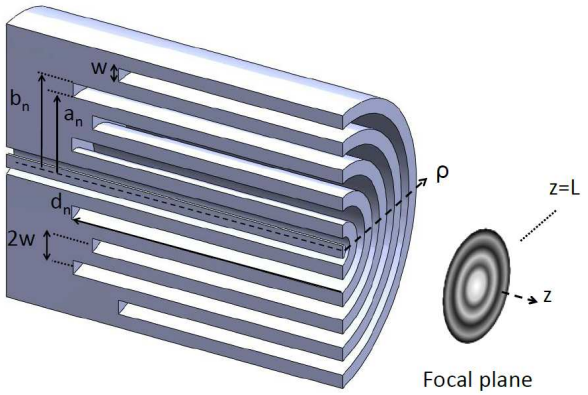

Figure 4.1: A concentrically corrugated near-field plate. The concentric corrugations have uniform width and spacing, while their depths are varied non-periodically in order to shape the desired focal pattern at $z = L$.

compared to those numerically computed for the measurement setup. Furthermore, the near-field plate's experimental frequency response is shown to be consistent with simulation results. Also, 2-D plots of the beams emitted by both the near-field plate and the coaxial probe are compared. The comparison confirms that the beam diverges more rapidly from the coaxial probe than the near-field plate. The beam emitted from the near-field plate is confined over a larger operating distance (focal length). Finally, the near-field plate is used to create 1-D and 2-D images of two in-phase dipole (coaxial) sources separated by a subwavelength distance. The images obtained using the near-field plate exhibit significantly higher resolution than those using a conventional coaxial probe. These results demonstrate the concentric near-field plate's ability to serve as a coaxially-fed, high resolution near-field probe.

4.2 Design Procedure

The concentrically corrugated near-field plate depicted in Figure 4.1 has a coaxially-fed central aperture and N concentric, circular grooves. The grooves ($n = 1...N$) have uniform width w, inner radius a_n, and outer radius b_n, but their depths (denoted as d_1 to d_N) are non-periodically varied. For design purposes, the metallic surface into which the grooves are placed is assumed to be infinite in the x and y directions. In addition, each groove (n) is modeled as a magnetic frill (an annular ring of magnetic current) [48]:

$$\vec{M}_n(\rho) = \frac{-V_n}{\rho \ln(\frac{b_n}{a_n})}\hat{\phi} \tag{4.1}$$

that exists between $a_n \leq \rho \leq b_n$, where V_n represents the voltage across each frill. The magnetic frills are equivalent sources with complex amplitudes equal to the tangential electric field across the openings of the coaxially-fed aperture ($n = 0$) and concentric grooves ($1 \leq n \leq N$).

The procedure for designing the concentrically corrugated near-field plate consists of a few steps [18], and is similar to the design procedure for a near-field plate with linear corrugations discussed in the previous chapter. The first step is to find the complex values of V_n needed to produce the desired electric-field focal pattern (E_z^{focal}) at a focal length $z = L$ from the plate. In this chapter, the z-directed electric

field at the focal plane is assumed to be a subwavelength Airy pattern of the form:

$$E_z^{focal}(\rho) = E_z(z = L, \rho) = \frac{J_1(k_{max}\rho)}{k_{max}\rho} \tag{4.2}$$

where $k_{max} > k$ is the maximum radial wavenumber that comprises the focal pattern, and $k = 2\pi/\lambda$ is the wavenumber in free space. The wavenumber k_{max} dictates the resolution of the focal spot. By sampling the focal pattern at regular intervals, $\rho_m = 2mw$, E_z^{focal} can be expressed in terms of the magnetic frills as a matrix equation,

$$2\sum_{n=0}^{N} V_n f_{nm}(z = L, \rho = \rho_m) = E_z^{focal}(\rho_m) \tag{4.3}$$

where m is an integer from 0 to N, and $f_{nm}(z = L, \rho = \rho_m)$ is the z component of the electric field at $(z = L, \rho = \rho_m)$ produced by the n^{th} groove. It should be noted that since image theory is used to simplify the problem to magnetic frills radiating in free space, the magnetic frill amplitudes must be doubled. The expression for f_{nm} is given by Equation (12) in [48]. Through matrix inversion, the magnetic frill voltages V_n can be found from Equation (4.3) given a desired E_z^{focal}. These voltages, along with Equations (12), (20), and (21) in [48], allow the electric and magnetic field to be found anywhere in space.

The second step in the design process involves finding the azimuthal magnetic field, H_ϕ, at the center of each magnetic frill ($\rho = \rho_n = (a_n + b_n)/2$):

$$2\sum_{p=0}^{N} V_p g_{pn}(z = 0, \rho = \rho_n) = H_\phi(z = 0, \rho = \rho_n) \tag{4.4}$$

where $g_{pn}(z = 0, \rho = \rho_n)$ is the ϕ component of magnetic field produced by p^{th} groove at $(z = 0, \rho = \rho_n)$, computed using Equation (21) in [48].

The third step estimates the impedance seen at the opening of each groove from the quantities M_n and H_ϕ:

$$\eta_n = \frac{M_n(\rho_n)}{H_\phi(z = 0, \rho_n)} \text{ for } 1 \leq n \leq N \tag{4.5}$$

where the relationship between the computed V_n and M_n values is given by Equation (4.1), and ρ_n is the same as in Equation (4.4).

The final step of the design procedure entails determining the depths d_n of the grooves ($n = 1$ to N) needed to realize the required values of η_n. This is achieved through scattering simulations. In the scattering simulations, the impedance (η_n) of a groove is extracted from normal incidence on an infinite array of linear grooves with identical widths w and depths. It should be noted that corrugations can only realize reactive impedances. However, since the real part of the required surface impedances is small, it is neglected (see chapter 2). In the design process, the fields in the space $z > 0$ were of primary concern. This region will be referred to as region 1, and the space inside the coaxial cable as region 2 (see Figure 4.1). The fields in regions 1 and 2 can be related to each other through the continuity of the tangential electric and magnetic fields across the central ($n = 0$) coaxial aperture. Specifically, the incident current, I_{inc}, in the coaxial line (region 2) can be related to the field in region 1 through the following approximate expression,

$$2I_{inc} + \frac{V_0}{Z_0} = 2\pi\rho_0 H_\phi(z = 0, \rho_0) \tag{4.6}$$

which considers only the TEM mode within the coaxial cable. The variable Z_0 represents the characteristic impedance of the cable and $\rho_0 = \rho_n$ in Equation (4.4) when $n = 0$. In summary, Equations (4.3), (4.4) and (4.5) can be used to directly relate the incident current (I_{inc}) in the coaxial cable to E_z^{focal}.

4.3 Simulation Results

As an example, we consider a concentrically corrugated near-field plate designed to operate at a frequency of 1.0 GHz ($\lambda = 0.3$ m). Throughout this chapter, the dimensions are given in terms of the design wavelength, $\lambda = 0.3$ m. The design parameters were chosen to be: $N = 4$, $L = \lambda/15$, $w = \lambda/80$ and $k_{max} = 8\pi k$. The central coaxial feed dimensions were $a_0 = 0.635$ mm and $b_0 = 2.05$ mm, which correspond to standard semi-rigid coaxial cable dimensions. The design parameters, N, w, L, a_n, and b_n were chosen by taking into account fabrications constraints and design procedure assumptions. The described plate produces a subwavelength Airy pattern at the focal plane with a null-to-null beamwidth of $\lambda/20$. It should be noted w, a_n, and b_n have been chosen such that the distance between adjacent magnetic frills (grooves) is less than half of the smallest feature size of the desired focal pattern. The frill voltages, V_n, and required groove depths, d_n, are found following the design procedure presented in the previous section, and are listed in Table 4.1 [20].

It should be noted that the signs of the voltage phases for adjacent elements (frills) are reversed, which is a characteristic feature of a near-field plate's aperture field, as mentioned earlier in chapters 2 and 3. It is also reminiscent of the aperture field of superdirective antenna arrays [49]. In both structures, the rapid phase variation increases the reactive power compared to that radiated, resulting in a high quality factor, Q [13, 49]. Due to this high Q, both near-field plates and superdirective antenna arrays are narrowband (see [49] and [19]). They possess small input resistances and large input reactances, resulting in a significant input impedance mismatch. While near-field plates and superdirective antenna arrays share these features, they are also distinct. Primarily, near-field plates produce a prescribed subwavelength near-field pattern, while superdirective antenna arrays produce a far-field pattern that is more directive than that produced by a uniformly excited aperture of the same size. Further, since near-field plates operate in the near field and superdirective arrays in the far field, they are designed using entirely different procedures. The difference is evident from a comparison of the step-by-step design procedure for near-field plates outlined in this chapter and previous chapters with that used to design superdirective arrays [50]. While several different experimental near-field plates have been presented in this report [14, 19, 20], superdirective antenna arrays have remained difficult to realize [51, 52]. One reason is that the tolerances on the magnitude and phase of the element excitations are exceedingly tight, making the feed extremely challenging to implement. Since near-field plates operate in the reactive near field, these tolerances are less stringent, simplifying fabrication. Superdirective antennas with passive reflectors or parasitic elements have also been pursued recently. Superdirective reflector arrays and parasitic arrays of electrically-small antennas were designed in [51, 53] and [52], respectively. Much like in near-field plates, mutual coupling between elements was exploited to minimize the complexity and loss of the feeding structure. These superdirective arrays, however, are still quite distinct from near-field plates. They are composed of identical, resonant elements that generate a superdirective far-field pattern, while the elements of a near-field plate are non-periodically varied to produce a subwavelength near-field pattern.

The designed near-field plate was then simulated in Comsol Multiphysics. In the simulations, the lossless metallic plate into which the grooves are placed is truncated to a radius of $\rho = 0.125\lambda$. The

Groove Index (n)	Normalized Voltage (V_n/V_{inc})	Groove Depth (d_n/λ)
0	$1.9999\angle 0.0635°$	NA
1	$0.0830\angle -179.9026°$	0.2412
2	$0.0252\angle 0.2079°$	0.241
3	$0.0080\angle -179.4839°$	0.2411
4	$0.0016\angle 1.4271°$	0.2425

Table 4.1: The groove voltages and depths for the near-field plate depicted in Figure 4.1. The voltages are normalized to the incident voltage computed using Equation (4.6), where $V_{inc} = Z_0 I_{inc}$ (from [20]).

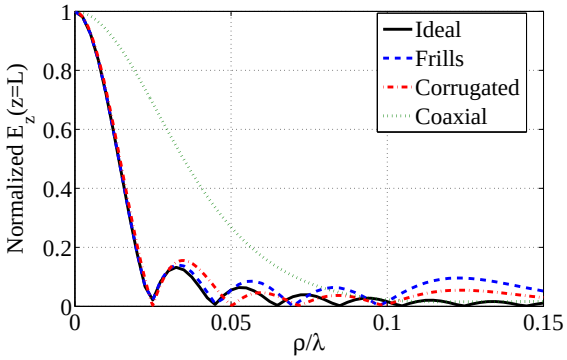

Figure 4.2: A subwavelength Airy function (*Ideal*) and z-directed electric-field focal patterns that approximate it. The *Frills* plot represents the focal pattern produced by the computed magnetic frills, while the *Corrugated* pattern represents the focal pattern formed by the lossless, concentrically corrugated near-field plate shown in Figure 4.1. The *Corrugated* pattern shows a null-to-null beamwidth of $\lambda/20$ at a focal length $z = L = \lambda/15 = 0.02$ m, where $\lambda = 0.3$ m. The *Corrugated* and *Coaxial* patterns are plotted for a frequency 1.195% above the design frequency (1 GHz) (from [20]).

simulated focal pattern (*Corrugated*) produced by the near-field plate is shown in Figure 4.2 along with the ideal subwavelength Airy pattern (*Ideal*). In addition, the focal pattern generated by the computed magnetic frills (*Frills*) is plotted. The *Frills* and *Ideal* patterns differ since the *Ideal* pattern was slightly undersampled when the frill voltages, V_n, were found using Equation (4.3). The slight difference between the *Corrugated* and *Frills* patterns results from the definition of the groove impedance, which assumes that the magnetic current across each groove is constant. In reality, the magnetic current varies slightly and its variation is given by Equation (4.1). Further, the formulas from [48] used to find the fields due to the magnetic frills are approximate, which also leads to the slight differences between the simulated *Corrugated* pattern and the *Frills* pattern. The simulated design is at a frequency 1.195% higher than that predicted by the approximate formulas. Finally, to emphasize the narrowness of the focal pattern produced by the designed plate, Figure 4.2 shows a plot (*Coaxial*) of the z-directed electric field pattern produced by the isolated ($n = 0$) coaxial aperture in a ground plane without corrugations. It should be noted that both *Coaxial* and *Corrugated* patterns are subwavelength in size, since the focal plane is within the structure's near field. However, at this same focal distance, the concentric corrugations allow for a significantly narrower spot.

To observe the effect of losses on the near-field plate's performance, the plate was also resimulated

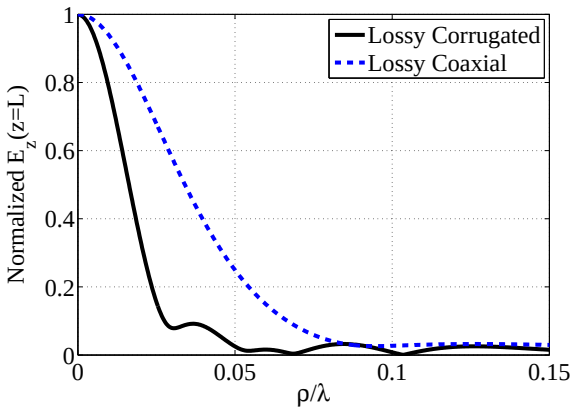

Figure 4.3: The focal pattern produced by the concentrically corrugated near-field plate with aluminium boundaries (solid line) versus the focal pattern produced by a coaxial aperture in an aluminium ground plane without corrugations. These results were computed using Comsol Multiphysics at a frequency 1.195% above the design frequency (1 GHz) (from [19]).

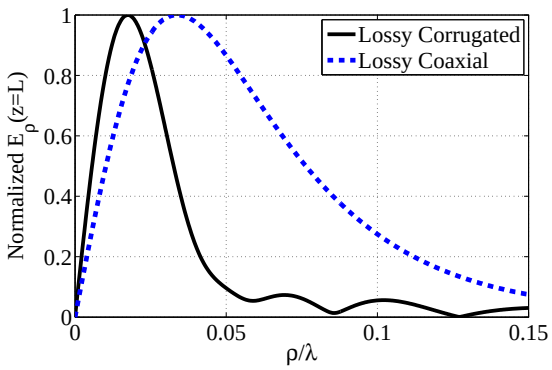

(a) ρ component

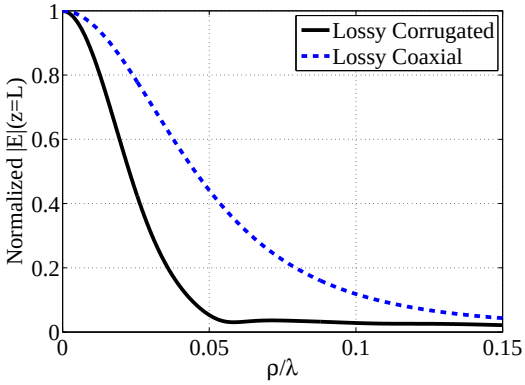

(b) magnitude

Figure 4.4: Simulated electric field at $z = L = 20$ mm from the concentrically corrugated near-field plate (denoted as *Corrugated*) and a coaxial probe (denoted as *Coaxial*). (a) Normalized ρ component of the electric field. (b) Normalized norm of the electric field (from [19]).

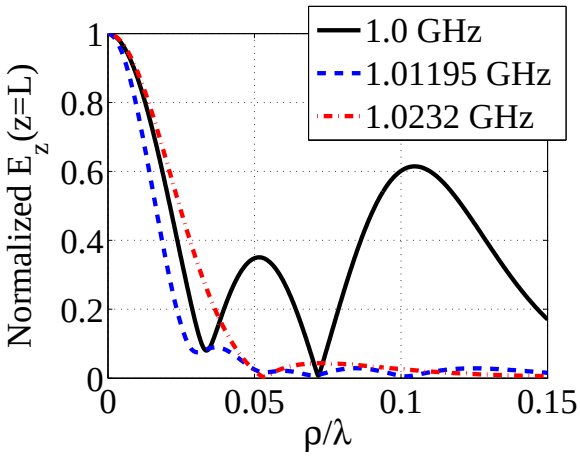

Figure 4.5: The concentrically corrugated near-field plate's frequency response. The near-field plate's operating frequency is 1.01195 GHz.

with a finite conductivity equal to that of aluminium. The focal pattern for the lossy plate is shown in Figure 4.3. The simulation results demonstrate that practical losses at microwave frequencies have a minimal effect on the beamwidth of the subwavelength focal pattern formed by the device. The ρ-component and norm of the electric field are also shown in Figure 4.4. Although the goal was to make a narrow E_z focal pattern, the norm of the electric field (Figure 4.4 (b)) formed by the concentric near-field plate is also significantly narrower than that of a coaxial probe.

Finally, the frequency response of the near-field plate is presented in Figure 4.5. Below the operating frequency, the side lobe levels increase significantly and the beamwidth fluctuates with decreasing frequency. In contrast, above the operating frequency, the side lobes are suppressed and the main beam widens with increasing frequency. For example, the FWHM which is $\lambda/30.73$ at the operating frequency 1.01195 GHz increases by 50% as the frequency is raised to 1.0232 GHz (1.11% increase in frequency).

In the next section, the fabricated structures and setup used to measure them are described in detail. Electric field measurements for both a simple coaxial probe and the concentrically corrugated near-field plate of equal dimensions are compared. It is shown that the simulated and experimental results are in close agreement, thereby validating the design procedure of the concentric near-field plate and its performance.

4.4 Measurements

The experimental setup used to measure the z-directed electric field patterns produced by the concentric near-field plate is illustrated in Figure 4.6. In the setup, a semi-rigid probe with an inner conductor radius of 0.46 mm and outer conductor radius of 1.8 mm was used to detect the near-field plate's electric-field patterns. The inner conductor of the semirigid probe was extended 4.5 mm to increase the signal strength received by the probe. The distance between the outer conductor of the semirigid probe and the surface of the corrugated plate was considered the measurement distance. Therefore, to measure a focal pattern at $z = L = \lambda/15 = 20$ mm, the semirigid probe was placed such that its outer conductor was 20 mm from the surface of the near-field plate. In the experiments, the semirigid probe was moved using an automated xyz translation stage.

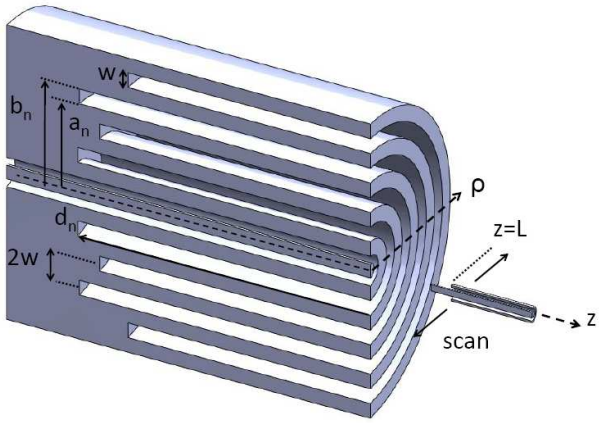

Figure 4.6: A concentrically corrugated near-field plate and the semirigid probe used to measure the electric patterns (from [20]).

The designed near-field plate was fabricated with a 12.5 micron (0.5 mil) accuracy by electric discharge machining (EDM) an aluminium cylinder (see Figure 4.7 (a)). For comparison purposes, a coaxial probe of equal dimensions, consisting of a single coaxial aperture without corrugations, was also fabricated, as shown in Figure 4.7 (b). At the experimental frequency of 1.0105 GHz, the reflection coefficient of the concentrically corrugated near-field plate was measured to be -0.75 dB. Such a high reflection coefficient is expected, given that the feed of the near-field plate terminates in an open circuit. However, when the near-field plate is used as a probe in the following section, a lower reflection coefficient was needed to increase its sensitivity: the received signal strength. Therefore, the near-field plate was matched using a double stub tuner to obtain a reflection coefficient of -6.5 dB at 1.0105 GHz. In addition, the semirigid probe used in the measurement setup (shown in Figure 4.6) was also matched using a double stub tuner to a reflection coefficient of -13.3 dB.

The simulated and measured electric (E_z) near-field patterns along the focal plane ($z = L = 20$ mm) of the near-field plate are shown in Figure 4.8 (a). The experimental focal pattern formed by the near-field plate is labeled *Corrugated Measurement* and exhibits a FWHM of $\lambda/23.58$. At the same distance, the experimental pattern formed by the coaxial probe (without corrugations) is labeled *Coaxial Measurement*. This pattern exhibits a FWHM of $\lambda/13.14$, which is 1.79 times wider than that produced by the near-field plate. Plotted in Figure 4.8 (a), is also a third pattern labeled *Corrugated Simulation*. It is the simulated focal pattern of the near-field plate detected by the semirigid probe along the focal plane $z = L = 20$ mm. It is computed using the Ansoft HFSS finite element electromagnetic solver. Similarly, *Coaxial Simulation* is the simulated electric-field pattern of the coaxial probe detected by the semirigid probe at the same distance. Both *Corrugated Simulation* and *Coaxial Simulation* show good agreement with the measured patterns, but clearly differ from the E_z patterns plotted in Figure 4.3. The difference is due to the fact that the semirigid probe, used to obtain the simulation and measurement results of Figure 4.8, slightly couples to the ρ component of the electric field in addition to the z component. Furthermore, the finite radius and length of the semirigid probes inner conductor slightly averages the electric field in both the ρ and z directions. The simulation of Figure 4.8 accurately capture the limitations of the semirigid probe used in experiment.

It should be noted that the HFSS simulations are reported at the design frequency of 1.01195 GHz, while the experimental results are reported at 1.0105 GHz: the fabricated plate's operating frequency.

(a) Corrugated near-field plate

(b) Coaxial probe

Figure 4.7: (a) A concentrically corrugated near-field plate fabricated from an aluminum cylinder using sink EDM. The near-field plate is fed by an SMA connector from the bottom side. (b) A coaxial probe consisting of a coaxial aperture in a cylindrical aluminum cylinder fed by an SMA connector from the bottom side (from [20]).

This 0.14% frequency shift can be attributed to the 12.5 μm tolerance of the EDM process used to fabricate the near-field plate. Figures 4.8 (b) and 4.8 (c) show the simulated and measured electric-field patterns at $z = 3L/4 = 15$ mm and $z = L/2 = 10$ mm respectively. Once again, the measurement results show excellent agreement with simulation. Finally, it should be pointed out that the measured pattern for the matched near-field plate and semi-rigid probe is 7 dB higher than the measured pattern for the unmatched case at the same distance.

In Figure 4.9, the electric field pattern measured at $z = 10$ mm is plotted for different frequencies. Below the operating frequency (1.0105 GHz), the electric field pattern produced by the corrugated plate shows ripples with no main beam, while above the operating frequency the main beam widens with increasing the frequency. This frequency dependance follows that described in simulation in the previous section.

To demonstrate the near-field plate's ability to confine the electromagnetic near-field to a symmetric narrow spot, the measured 2-D electric field patterns at $z = 15$ mm for both the corrugated near-field plate and the coaxial probe are depicted in Figure 4.10. Finally, the emitted beam from the coaxial probe and the corrugated near-field plate are compared in Figure 4.11. In the plot, the measured electric field (E_z) along each $z = z'$ plane has been normalized to its corresponding maximum value: $E_z(\rho, z = z')/E_z(\rho = 0, z = z')$. These two figures confirm the superior ability of the near-field plate to confine the electromagnetic near field over an extended operating distance. In the next section, the electromagnetic confinement provided by the near-field plate is used to resolve two sources separated by a subwavelength distance.

4.5 Detection of Sources

Figure 4.10 demonstrates that the concentrically corrugated near-field plate produces higher resolution focal spots than a conventional coaxial probe. This suggests that the near-field plate could also provide higher resolution when imaging sources. To test this, two similar dipole sources (coaxial) separated by distance s were placed at distance $z = 15$ mm from the near-field plate. The distance s is defined as the

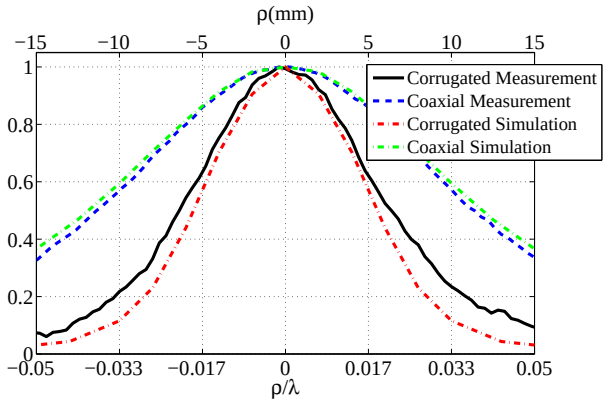

(a) $z = 20$ mm

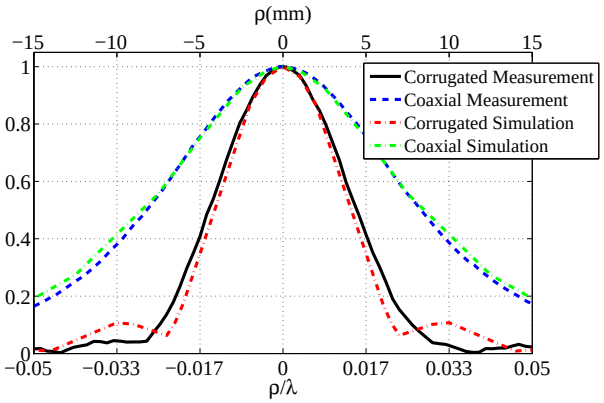

(b) $z = 15$ mm

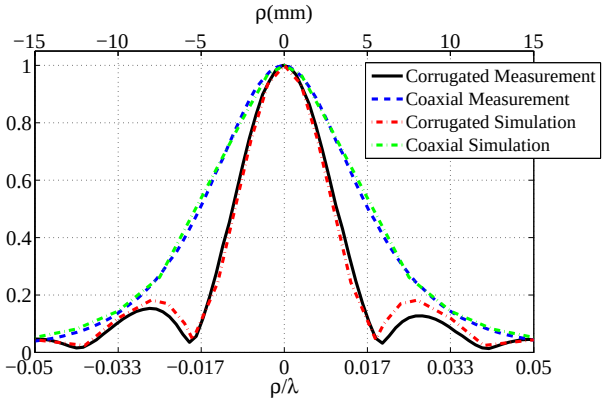

(c) $z = 10$ mm

Figure 4.8: (a) Electric near-field patterns at $z = 20$ mm formed by the concentric near-field plate and detected using the measurement set up shown in Figure 4.6. *Corrugated Measurement* and *Coaxial Measurement* are the measured near-field patterns formed by the impedance matched concentrically corrugated plate and coaxial probe, respectively. *Corrugated Simulation* and *Coaxial Simulation* are the corresponding simulated near-field patterns. (b) Electric near-field patterns at $z = 15$ mm. (c) Electric near-field patterns at $z = 10$ mm. The simulation results include dielectric and conductor losses (from [20]).

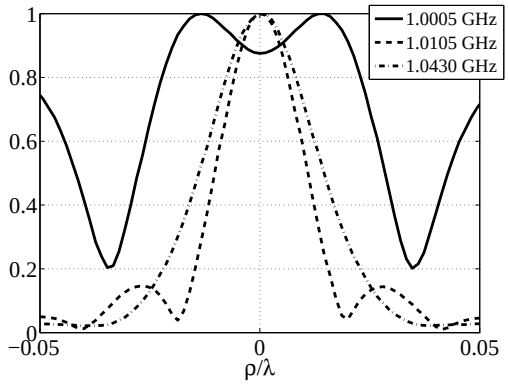

Figure 4.9: Measured near-field patterns generated by the concentrically corrugated near-field plate at $z = 10$ mm for different frequencies. The near-field plate's operating frequency is 1.0105 GHz (from [20]).

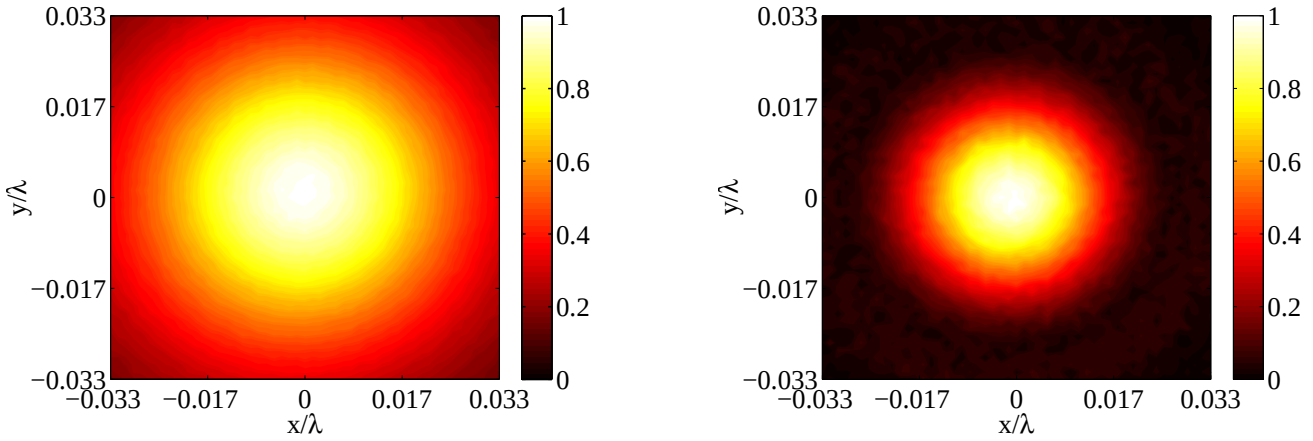

(a) Coaxial probe

(b) Near-field plate

Figure 4.10: Measured two-dimensional focal patterns ($z = 15$ mm) produced by (a) the coaxial probe and (b) the concentrically corrugated near-field plate (from [20]).

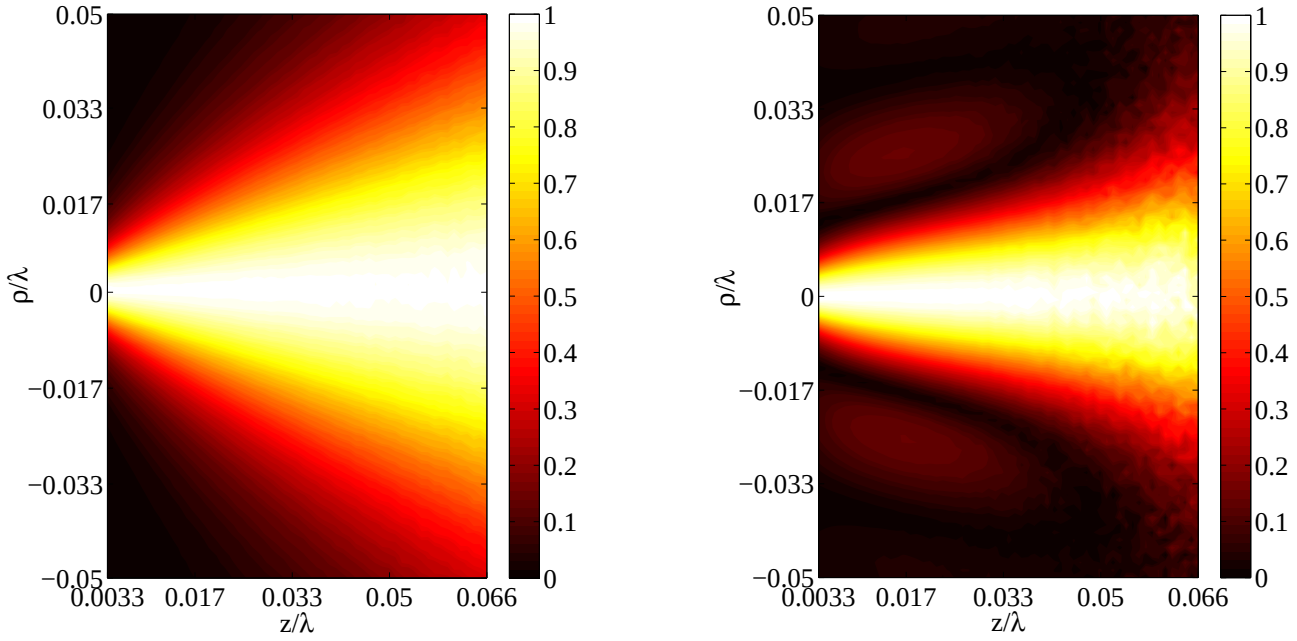

(a) Coaxial probe

(b) Near-field plate

Figure 4.11: Measured beam emitted from (a) the coaxial probe and (b) the concentrically corrugated near-field plate. In both plots, the measured field along each $z = z'$ plane is normalized to its maximum value: $E_z(\rho, z = z')/E_z(\rho = 0, z = z')$. The near-field patterns along $z = 0.066\lambda = 20$ mm, $z = 0.05\lambda = 15$ mm, and $z = 0.033\lambda = 10$ mm are plotted in Figure 4.8 (from [20]).

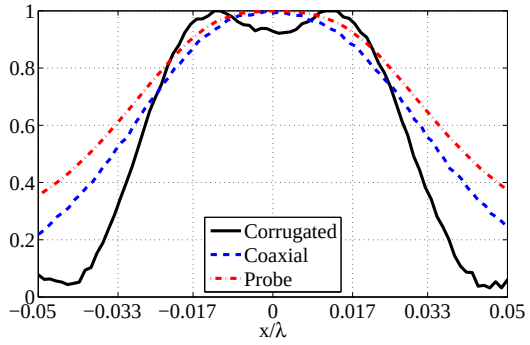

(a) separation distance $s = 9.1 \text{ mm} = \lambda/33$

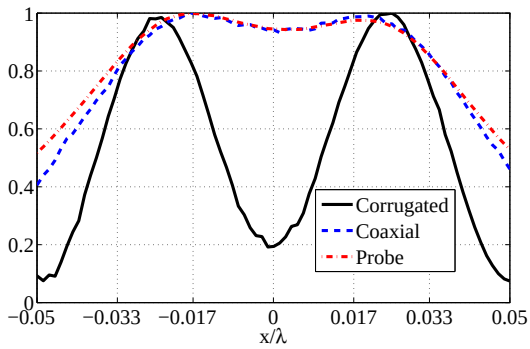

(b) separation distance $s = 13.8 \text{ mm} = \lambda/21.74$

Figure 4.12: Resolving two dipole (coaxial) sources located at $z = 15$ mm and separated by (a) $s = 9.1 \text{ mm} = \lambda/33$ and (b) $s = 13.8 \text{ mm} = \lambda/21.74$ along the x axis ($y = 0$). The plot labeled *Corrugated* denotes the electric near-field pattern measured using the concentrically corrugated near-field plate. The plot labeled *Coaxial* denotes the pattern measured using the coaxial probe. The plot labeled *Probe* denotes the pattern measured using a semirigid coaxial probe (with inner radius 0.52 mm, outer radius 2.20 mm, and a 5.2 mm extended inner conductor) (from [20]).

distance between the centers of the two dipole sources. The concentrically corrugated near-field plate and the coaxial probe were used to image the two sources by detecting the field emitted by the sources. Figure 4.12 shows the detected patterns for two different separation distances s. The pattern measured by the near-field plate is denoted as *Corrugated*, while *Coaxial* denotes the pattern measured by the coaxial probe. For comparison purposes, the pattern measured by a simple semi-rigid probe (with inner radius 0.52 mm, outer radius 2.20 mm, and a 5.2 mm extended inner conductor) is also shown in Figure 4.12, and denoted as *Probe*.

Figure 4.12 (a) shows the extreme case when the sources cannot be resolved by the coaxial probe. In this figure, the sources have been placed $s = 9.1 \text{ mm} = \lambda/33$ apart. In contrast, the near-field plate can distinguish the two sources at the same separation distance (see Figure 4.12(a)). The distance between the two peaks measured by the corrugated near-field plate is $7.9 \text{ mm} = \lambda/38$, while the separation between the two sources is $s = 9.1 \text{ mm} = \lambda/33$. The difference is due to mutual interaction of the two sources. The 2-D patterns measured using the near-field plate and the coaxial probe are shown in Figure 4.13. The two sources are easily distinguishable from the pattern measured by the near-field plate, while the pattern measured by the coaxial probe shows only one source.

Figure 4.12 (b) shows another extreme case, where the two sources are resolvable by the coaxial probe. In this case, the two sources are placed $s = 13.8 \text{ mm} = \lambda/21.74$ apart. It is evident that the near-field plate can resolve the two sources completely, while the coaxial probes can only distinguish between them. The separation between the two sources observed using the corrugated near-field plate is $14.2 \text{ mm} = \lambda/21.1$, which is very close to the physical separation distance of $s = 13.8 \text{ mm} = \lambda/21.74$. The slight difference is due to the finite step size taken by the xyz-translation stage used in the measurement setup. The higher resolution obtained using the corrugated near-field plate in resolving the two sources is more pronounced in the 2-D patterns shown in Figure 4.14.

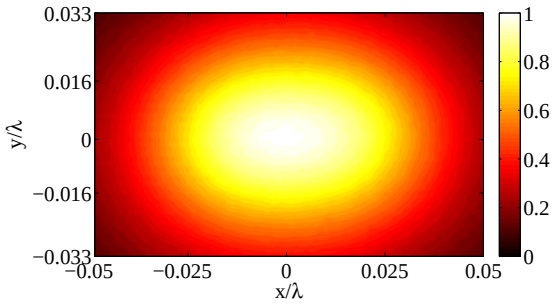

(a) Coaxial probe

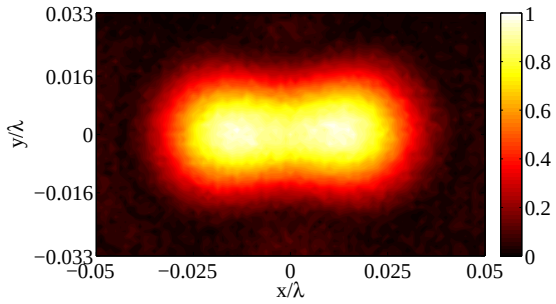

(b) Near-field plate

Figure 4.13: Resolving two dipole sources (coaxial) located at $z = 15$ mm and separated by $s = 9.1$ mm $= \lambda/33$. (a) Two-dimensional electric near-field pattern measured using the coaxial probe. (b) Two-dimensional pattern measured using the corrugated near-field plate (from [20]).

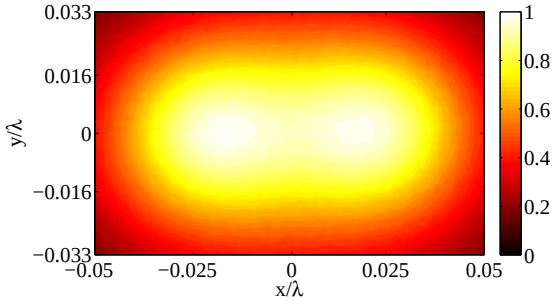

(a) Coaxial probe

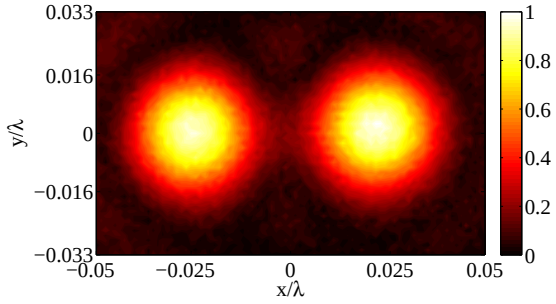

(b) Near-field plate

Figure 4.14: Resolving two dipole sources (coaxial) located at $z = 15$ mm and separated by $s = 13.8$ mm $= \lambda/21.74$. (a) Two-dimensional electric near-field pattern measured using the coaxial probe. (b) Two-dimensional pattern measured using the corrugated near-field plate (from [20]).

4.6 Conclusion

In this chapter, a concentrically corrugated near-field plate was studied both in simulation and measurement. A step-by-step design procedure was outlined and simulation results were presented that confirm the ability of the designed near-field plate to create a 2-D focus. The effect of practical losses on the performance of the near-field plate was shown to be minimal, and its frequency response was also studied. Furthermore, the experimental performance of an impedance matched concentrically corrugated near-field plate possessing four grooves was investigated. The electric field patterns produced by the corrugated plate and a simple coaxial probe (without corrugations) of the same dimensions were measured at different focal distances at approximately 1 GHz and compared. The subwavelength electric-field pattern produced by the corrugated near-field plate at $z = \lambda/15 = 20$ mm was shown to possess a FWHM that is 1.79 times narrower than that of the coaxial probe. Measurement and simulation results were shown to be in close agreement, thus validating the design procedure. In addition, the beam emitted by the corrugated near-field plate was significantly narrower than that emitted by the coaxial probe, thus confirming the near-field plate's superior ability to confine electromagnetic field over a focal length (an extended operating distance). Finally, the near-field plate was used to image two coaxial sources placed a subwavelength distance apart. The images obtained using the near-field plate exhibited significantly higher resolution than those obtained using the coaxial probe. The results reported in this chapter demonstrate that non-periodic, concentrically corrugated surfaces can provide new opportunities to develop high resolution near-field probes and sensors.

5.0

Summary and Applications

5.1 Summary

This report investigated near-field plates as an alternative method of overcoming the diffraction limit [11]. Near-field plates are non-periodic, engineered surfaces that can form subwavelength focal patterns. In [12], their step-by-step design procedure was outlined and a realization consisting of a purely reactive modulated surface impedance was proposed. In [14], the first experimental realization of a near-field plate was reported.

In this report, we first characterized near-field plates analytically to gain insight into their operation. In the analytical treatment, distinctive features of a near-field plate and its operation were described in detail. It was shown that near-field plates can be realized using purely reactive (passive) surface impedances. Next, the first experimental near-field plate was described. The fabricated plate consisted of an array of interdigitated capacitors. In experiment, the plate was shown to focus the radiation emanating from a cylindrical source to a 1-D electric-field focal pattern with $\mathrm{FWHM} = \lambda/18$ at approximately $1\ \mathrm{GHz}$. Close agreement between full-wave simulation and measurement was demonstrated.

In the remainder of the report, novel near-field plate configurations suitable for practical use were presented. The first configuration was a linearly corrugated near-field plate. It consisted of a slit in a metallic slab (parallel plate waveguide) surrounded by non-periodic symmetric linear corrugations. The non-periodic corrugations acted as parasitic radiators which tailored the electromagnetic near field emitted from the central slit. The width and spacing of the grooves were chosen to be uniform, while their depth was non-periodically varied to shape the subwavelength 1-D magnetic-field focal pattern. A design procedure for such a device was outlined. Two different examples of corrugated near-field plates were designed and studied through full-wave simulation. The effect of losses was also considered, and two different methods to reduce reflection from the near-field plate were demonstrated. Furthermore, an experimental corrugated near-field plate was also studied. Simulation and free-space measurements were reported at approximately $10\ \mathrm{GHz}$, confirming the corrugated plate's ability to form a subwavelength focus with $\mathrm{FWHM} = \lambda/9.23$ at a distance $\lambda/15$ from the output face of the plate.

The second configuration investigated was a concentrically corrugated near-field plate. It was fed through a coaxial cable and formed a 2-D subwavelength focal pattern. This plate consisted of a coaxial aperture in a metallic surface surrounded by non-periodic concentric corrugations. The concentric corrugations had uniform width and spacing, while their depths were designed to form a prescribed 2-D subwavelength electric-field focal pattern. The plate's design procedure was outlined and verified through full-wave simulation. Furthermore, the experimental performance of an impedance matched

concentrically corrugated near-field plate possessing four grooves was investigated. The electric near-field patterns produced by the corrugated plate and a simple coaxial probe (without corrugations) of the same dimensions were measured at approximately 1 GHz and compared. The subwavelength electric-field pattern produced by the corrugated near-field plate at $z = \lambda/15 = 20$ mm was shown to possess a FWHM that is 1.79 times narrower than that of the coaxial probe. Also, measurement and simulation results were shown to be in close agreement, thus validating the procedure used to design the near-field plate. In addition, the beam emitted by the corrugated near-field plate was significantly narrower than that emitted by the coaxial probe, thus confirming the plate's superior ability to confine electromagnetic field over a focal length (an extended operating distance). Finally, the near-field plate was used to image two coaxial sources placed a subwavelength distance apart. The images obtained using the near-field plate exhibited significantly higher resolution than those obtained using the coaxial probe.

In addition to confirming a near-field plate's ability to overcome the diffraction limit, this report also demonstrated several advantages offered by near-field plates. It was shown that near-field plates can be designed for various excitations. For example, near-field plates fed by cylindrical sources, parallel plate waveguides, plane waves, and a coaxial cable excitation were reported. It was also shown that near-field plates can be modified depending on their application to produce subwavelength focal patterns with desired polarizations of electric or magnetic field. For instance, the near-field plate in chapter 3 formed a 1-D magnetic-field focal pattern while the near-field plate in chapter 4 produced a 2-D z-directed electric-field focal pattern. Furthermore, different methods of reducing the reflection from near-field plates were demonstrated. Finally, it was reported that near-field plates were robust to practical losses and exhibited a $1 - 2\%$ frequency bandwidth, which is acceptable in many applications. Because of these advantages, which are not offered by other similar structures such as negative refractive index metamaterials or near-field probes, near-field plates will find applications in several areas.

5.2 Applications

Near-field probes and subwavelength focusing devices based on near-field plates, that generate subwavelength beam waists or focal patterns, will find numerous applications [21]. Research on near-field plates may lead to advances in biomedical devices, microscopes with unprecedented resolution, lithography systems that allow unparalleled levels of electronic integration, as well as improvements to existing wireless power transfer systems.

The near-field plate's ability to manipulate the near field and provide strong spatial confinement could be leveraged to improve the performance of near-field sensors. A near-field plate has a larger operating distance (focal length) than a conventional near-field probe (as demonstrated in chapters 3 and 4). Therefore, a given subwavelength resolution can be maintained at a greater distance than would be possible using a conventional probe. The subwavelength focus formed by a near-field plate when transmitting, allows it to detect over the same narrow spot when used as a receiver or probe. For microscopy and lithography applications, the availability of sub-micron and sub-nanometer feature fabrication techniques could allow arbitrarily high resolutions.

Near-field plates may also find use in wireless non-radiative power transfer systems. Specifically, megahertz receiving and transmitting devices based on near-field plates could provide specific advantages over the resonant coils that have been used to date [54]. Near-field plates could be designed to provide magnetic field illumination to only certain areas of a confined environment, where electronic devices are typically placed. For example, tailored energy hotspots, or rather watt spots, could be established

on the top of desks or countertops using near-field plates. Near-field plates may also radiate less energy to the far field than the single or multi-turn loops used in wireless non-radiative power transfer systems due to the oscillatory (in and out-of-phase) currents supported by them. Finally, tailoring the magnetic near-field illumination with transmitting and receiving devices based on near-field plates may increase the range and efficiency of wireless power systems.

Near-field plates could conceivably be used to improve targeting capabilities in medical devices such as those used in transcranial magnetic stimulation (TMS) [55]. Specifically, the use of near-field plates may lead to increased electromagnetic field penetration while maintaining a small stimulated volume within the brain. In TMS, a time-varying magnetic field is used to induce an electromotive force within brain tissue in order to excite neurons. The super-resolving power of a near-field plate could perhaps be used to precisely direct neuronal stimulation in TMS.

At optical frequencies, near-field plates can be realized using plasmonic (inductive) and dielectric (capacitive) materials [25–28,56]. The microwave near-field plate designs presented in this report can be extended to optical frequencies using the concept of nanocircuit elements [57]. Nanostructured implementations hold promise for near-field optical data storage [58], near-field microscopy and lithography applications. Near-field plates could also be integrated into quasi-optical and optical systems as focusing or beam-shaping elements. For example, an incident beam could be focused to subwavelength spots (waists) prior to entering a millimeter-wave, THz, infrared or optical device. In this way, the size of system components could be significantly reduced. Such focusing elements may be used as light concentrators in infrared or optical detector arrays. Near-field plates could also be employed as beam-shaping devices. For instance, a Gaussian or Bessel beam could be generated from an elementary source using a near-field plate.

5.3 Publications

The following publications have resulted from this research effort.

Articles in Refereed Journals:

1. M. F. Imani and A. Grbic, "An experimental concentric near-field plate," *IEEE Transactions on Microwave Theory and Techniques*, to appear in December 2010.

2. A. Grbic, R. Merlin, E. M. Thomas, M. F. Imani, "Near-field plates: Metamaterial surfaces / arrays for subwavelength focusing and probing," *Proceedings of the IEEE*, to appear in 2011 (Special Issue on Metamaterials: Fundamentals and Applications in the Microwave and Optical Regimes).

3. M. F. Imani and A. Grbic, "An analytical investigation of near-field plates," *Metamaterials*, vol 4. pp. 104-111, Aug.-Sept. 2010 (Metamaterials 2009 Congress Special issue).

4. M. F. Imani and A. Grbic, "Tailoring near-field patterns with concentrically corrugated plates," *Applied Physics Letters*, vol. 95, pp. 111107, September 2009.

5. M. F. Imani and A. Grbic, "Near-field focusing with a corrugated surface," *IEEE Antennas and Wireless Propagation Letters*, vol. 8, 421-424 pages, May 2009.

6. A. Grbic and R. Merlin, "Near-field focusing plates and their design," *IEEE Transactions on Antennas and Propagation*, vol. 56, no. 10, pp. 3159-3165, October 2008.

7. A. Grbic, L. Jiang, R. Merlin, "Near-field plates: Subdiffraction focusing with patterned surfaces," *Science*, vol. 320, no. 5874, pp. 511-513, April 25, 2008.

Conference Proceedings:

1. M. F. Imani and A. Grbic, "A concentrically corrugated near-field plate," *IEEE MTT-S International Microwave Symposium Digest*, pp. 1648-1651, May 2010.

2. M. F. Imani and A. Grbic, "Design and implementation of near-field plates," *International Conference on Advanced Electromagnetic Materials in Microwaves and Optics (Metamaterials 09)*, 3 pages, August 2009 (invited).

3. M. F. Imani and A. Grbic, "Subwavelength focusing with a corrugated metallic plate," *IEEE Antennas and Propagation Society International Symposium*, 4 pages, June 2009.

4. R. Merlin, L. Jiang and A. Grbic, "Near-field plates: Subwavelength focusing and radiationless interference," *International Conference on Advanced Electromagnetic Materials in Microwaves and Optics (Metamaterials 08)*, 3 pages, September 2008 (invited).

5. M. F. Imani and A. Grbic, "An analytical investigation of near-field plates," *XXIX General Assembly of the International Union of Radio Science (URSI)*, August 2008 (invited).

6. A. Grbic, L. Jiang and R. Merlin, "Near-field focusing plates," *IEEE MTT-S International Microwave Symposium Digest*, pp. 209212, June 2008.

7. A. Grbic, L. Jiang and R. Merlin, "Near-field focusing plates: Theory and experiment," *Conference on Lasers and Electro-Optics and Quantum Electronics and Laser Science (CLEO QELS)*, 2 pages, May 2008.

5.4 Patent Disclosures During Reporting Period

- Patent Title: Apparatus for Sub-wavelength Near-field Focusing of Electromagnetic Waves.
  Inventors: Roberto Merlin and Anthony Grbic
  Provisional Patent (Application No. 60/938,858) filed May 18 2007.
  Patent (U.S. Application Serial No. 12/123,434) filed May 19, 2008.
  Assignee: Regents of the University of Michigan, Office of Technology Transfer,
  Wolverine Tower, Room 2071, South State Street, Ann Arbor, MI, 48109-1280.

5.5 Honors/Awards Received

The following awards were received by the PI and his graduate student during the course of this research work.

Anthony Grbic

1. Henry Russel Award, University of Michigan, to be received in March 2011.

2. Presidential Early Career Award for Scientists and Engineers (PECASE), 2010-2015.

Mohammadreza F. Imani

1. Finalist in the Student Paper Competition, IEEE International Symposium on Antennas and Propagation, Charleston, SC, USA, 2009.

2. Second place in the "Waves, Simulation and Radiation" session of the University of Michigan Engineering Graduate Symposium, 2008.

Bibliography

[1] E. H. Synge, "A suggested method for extending the microscopic resolution into the ultramicroscopic region," *Philosophical Magazine*, vol. 6, pp. 356–362, 1928.

[2] E. A. Ash and G. Nicholls, "Super-resolution aperture scanning microscope," *Nature*, vol. 237, pp. 510–511, 1972.

[3] L. Novotny, B. Hecht, *Principles of Nano-Optics*, Cambridge Press, London, 2006.

[4] S. M. Anlage, V. V. Talanov, A. R. Schwartz, *Principles of Near-Field Microwave Microscopy*, Springer-Verlag, New York, 2007.

[5] J. B. Pendry, "Negative refraction makes a perfect lens," *Physical Review Letters*, vol. 85, pp. 3966–3969, October 2000.

[6] R. A. Shelby, D. R. Smith, and S. Schultz, "Experimental verification of a negative index of refraction," *Science*, vol. 292, pp. 77–79, April 2001.

[7] A. Grbic and G.V. Eleftheriades, "Overcoming the diffraction limit with a planar left-handed transmission-line lens," *Physical Review Letters*, vol. 92, pp. 117403, March 2004.

[8] D. Melville and R. Blaikie, "Super-resolution imaging through a planar silver layer," *Optics Express*, vol. 13, pp. 2127–2134, March 2005.

[9] N. Fang and H. Lee and C. Sun and X. Zhang, "Sub-diffraction-limited optical imaging with a silver superlens," *Science*, vol. 308, pp. 534–537, April 2005.

[10] F. Mesa, M.J. Freire, R. Marques, and J.D. Baena, "Three-dimensional superresolution in metamaterial slab lenses: Experiment and theory," *Physical Review B*, vol. 72, pp. 235117, December 2005.

[11] R. Merlin, "Radiationless electromagnetic interference: Evanescent-field lenses and perfect focusing," *Science*, vol. 317, pp. 927–929, July 2007.

[12] A. Grbic, R. Merlin, "Near-field focusing plates and their design," *IEEE Transactions on Antennas and Propagation*, vol. 56, pp. 3159–3165, October 2008.

[13] M. F. Imani and A. Grbic, "An analytical investigation of near-field plates," *Metamaterials*, vol. 4, no. 2-3, pp. 104–111, 2010, Metamaterials-2009 Congress in London.

[14] A. Grbic, L. Jiang, and R. Merlin, "Near-field plates: Subdiffraction focusing with patterned surfaces," *Science*, vol. 320, pp. 511–513, April 2008.

[15] A. Grbic, L. Jiang, and R. Merlin, "Near-field focusing plates," *IEEE MTT-S International Microwave Symposium (WE1A-02)*, vol. WE1A-02, pp. 209–212, June 2008.

[16] M.F. Imani and A. Grbic, "Near-field focusing with a corrugated surface," *Antennas and Wireless Propagation Letters, IEEE*, vol. 8, pp. 421 –424, 2009.

[17] M.F. Imani and A. Grbic, "Subwavelength focusing with a corrugated metallic plate," *Antennas and Propagation Society International Symposium, 2009. APSURSI '09. IEEE*, pp. 1–4, jun. 2009.

[18] M. F. Imani and A. Grbic, "Tailoring near-field patterns with concentrically corrugated plates," *Applied Physics Letters*, vol. 95, pp. 111107, September 2009.

[19] M.F. Imani and A. Grbic, "A concentrically corrugated near-field plate," *Microwave Symposium Digest (MTT), 2010 IEEE MTT-S International*, pp. 1648–1651, may. 2010.

[20] M. F. Imani and A. Grbic, "An experimental concentric near-field plate," *IEEE Transactions on Microwave Theory and Techniques*, accepted for publication, to appear in December 2010.

[21] A. Grbic, R. Merlin, E. M. Thomas, M. F. Imani, "Near-field plates: Metamaterial surfaces / arrays for subwavelength focusing and probing," *Proceedings of the IEEE, (invited to a Special Issue on Metamaterials: Fundamentals and Applications in the Microwave and Optical Regimes)*, accepted for publications, to appear in 2011.

[22] L. Markley and G. Eleftheriades, "A near-field probe for subwavelength-focused imaging," *IEEE MTT-S International Microwave Syposium*, pp. 281–284, June 2009.

[23] G. V. Eleftheriades and A. M. H. Wong, "Holography-inspired screens for sub-wavelength focusing in the near field," *IEEE Microwave and Wireless Component Letters*, vol. 18, pp. 236–238, April 2008.

[24] L. Markley, A. M. H. Wong, Y. Wang and G.V. Eleftheriades, "Spatially shifted beam approach to sub-wavelength focusing," *Physical Review Letters*, vol. 101, pp. 113901, September 2008.

[25] I. Tsukerman, "Superfocusing by nanoshells," *Optics Letters*, vol. 34, pp. 1057–1059, 2009.

[26] R. Gordon, "Proposal for superfocusing at visible wavelengths using radiationless interference of a plasmonic array," *Physical Review Letters*, vol. 102, pp. 207402, May 2009.

[27] H. Shi and L. J. Guo, "Design of plasmonic near field plate at optical frequency," *Applied Physics Letters*, vol. 96, pp. 141107, April 2010.

[28] Y. Wang, A. M. H. Wong, L. Markley, A. S. Helmy, and G. V. Eleftheriades, "Plasmonic metascreen for alleviating the trade-offs in the near-field optics," *Optics Express*, vol. 17, pp. 12351–12361, July 2009.

[29] T. B. A Senior and J. L. Volakis, *Approximate boundary conditions in electromagnetics*, Institution of Engineering and Technology, Edison, NJ, 1995.

[30] C. A. Balanis, *Advanced Engineering Electromagnetics*, John-Wiley and Sons, New York, 1989.

[31] M. Abramovitz, I.A. Stegun, *Handbook of Mathematical Functions with Formulas, Graphs, and Mathematical Tables*, Dover Publications, New York, 1970.

[32] T. W. Ebbesen, H. J. Lezec, H. F. Ghaemi, T. Thio1 and P. A. Wolff, "Extraordinary optical transmission through sub-wavelength hole arrays," *Nature*, vol. 391, pp. 667–669, February 1998.

[33] J. A. Porto, F. J. Garcia-Vidal, J. B. Pendry, "Transmission resonances on metallic gratings with very narrow slits," *Physical Review Letters*, vol. 83, pp. 2845–2848, October 1999.

[34] L. Martn-Moreno, F. J. Garca-Vidal, H. J. Lezec, K. M. Pellerin, T. Thio, J. B. Pendry, and T.W. Ebbesen, "Theory of extraordinary optical transmission through subwavelength hole arrays," *Physical Review Letters*, vol. 86, pp. 1114–1117, February 2001.

[35] H. J. Lezec, A. Degiron, E. Devaux, R. A. Linke, L. Martin-Moreno, F. J. Garcia-Vidal, T. W. Ebbesen, "Beaming light from a subwavelength aperture," *Science*, vol. 297, pp. 820–822, August 2002.

[36] L. Martn-Moreno, F. J. Garca-Vidal, H. J. Lezec, A. Degiron, and T. W. Ebbesen, "Theory of highly directional emission from a single subwavelength aperture surrounded by surface corrugations," *Physical Review Letters*, vol. 90, pp. 167401, April 2003.

[37] F. J. Garcia-Vidal, H. J. Lezec, T. W. Ebbesen, and L. Martin-Moreno, "Multiple paths to enhance optical transmission through a single subwavelength slit," *Physical Review Letters*, vol. 90, pp. 213901, May 2003.

[38] F. J. Garcia-Vidal, L. Martin-Moreno, H. J. Lezec, and T. W. Ebbesen, "Focusing light with a single subwavelength aperture flanked by surface corrugations," *Applied Physics Letters*, vol. 83, pp. 4500–4502, December 2003.

[39] M. J. Lockyear, A. P. Hibbins, J. R. Sambles, C. R. Lawrence, "Surface-topography-induced enhanced transmission and directivity of microwave radiation through a subwavelength circular metal aperture," *Applied Physics Letters*, vol. 84, pp. 2040–2042, March 2004.

[40] S. S. Akarca-Biyikli, I. Bulu, E. Ozbay, "Enhanced transmission of microwave radiation in one-dimensional metallic gratings with subwavelength aperture," *Applied Physics Letters*, vol. 85, pp. 1098–1100, August 2004.

[41] D.R. Jackson, A.A. Oliner, T. Zhao, and J.T. Williams, "The beaming of light at broadside through a subwavelength hole: Leaky-wave model and open stopband effect," *Radio Science*, vol. 40, pp. RS6S10, 2005.

[42] J. B. Pendry, L. Martin-Moreno, F. J. Garcia-Vidal, "Mimicking surface plasmons with structured surfaces," *Science*, vol. 305, pp. 847–848, August 2004.

[43] X. Luo, C. Wang. C. Du, H. Shi, H. Gao, J. Ma, Y. Fu, H. Li, "Beaming light from a subwavelength slit surrounded by an array of grooves with different depth," *Proc. SPIE*, vol. 5927, 2005.

[44] S. L. Ray A. F. Peterson and R. Mittra, *Computational Methods for Electromagnetics*, IEEE Press, Piscataway, NJ, 1998.

[45] D. M. Pozar, *Microwave Engineering*, John Wiley and Sons, Inc, New York, 2005.

[46] P. F. Goldsmith, *Quasioptical Systems: Gaussian Beam Quasioptical Propagation and Applications*, IEEE Press, Piscataway, NJ, 1998.

[47] S.M. Rudolph and A. Grbic, "Broadband, low-loss negative-permeability and negative-index media for free-space applications," *Microwave Symposium Digest, 2009. MTT '09. IEEE MTT-S International*, pp. 113 –116, jun. 2009.

[48] A. Sakitani, S. Egashira, "Simplified expressions for the near fields of a magnetic frill current," *IEEE Transactions on Antennas and Propagation*, vol. AP-34, pp. 1059, 1986.

[49] Constantine A. Balanis, *Antenna Theory: Analysis, and Design*, John-Wiley and Sons, New York, 2nd edition, 1996.

[50] R. C. Hansen, *Electrically Small, Superdirectivity, and Superconducting Antennas*, John-Wiley and Sons, New York, 2006.

[51] S.A. Bokhari, H.K. Smith, J.R. Mosig, J.F. Zurcher, and F.E. Gardiol, "Superdirective antenna array of printed parasitic elements," *Electronics Letters*, vol. 28, no. 14, pp. 1332 –1334, jul. 1992.

[52] A. D. Yaghjian, T. H. ODonnell, E. E. Altshuler, and S. R. Best, "Electrically small supergain end-fire arrays," *Radio Science*, vol. 43, RS3002, pp. 13, 2008.

[53] V. Veremey, "Superdirective antennas with passive reflectors," *Antennas and Propagation Magazine, IEEE*, vol. 37, no. 2, pp. 16 –27, apr. 1995.

[54] A. Kurs, A. Karalis, R. Moffatt, J.D. Joannopoulos, P. Fisher, and M. Soljacic, "Wireless power transfer via strongly coupled magnetic resonances," *Science*, vol. 317, pp. 83–86, July 2007.

[55] L. Hernandez-Garcia, S. Lee, and W. Grissom, "An approach to MRIbased dosimetry for transcranial magnetic stimulation," *NeuroImage*, vol. 36, pp. 1171–1178, July 2007.

[56] L. Scoranno, F. Bilotti and L. Vegni, "Desig of a meta-screen for nearzone field focalizatoin at optical frequencies," *Microwave and Optical Technology Letters*, vol. 51, pp. 2718–2721, November 2009.

[57] N. Engheta, A. Salandrino, and A. Alu, "Circuit elements at optical frequencies: nanoinductors, nanocapacitors, and nanoresistors," *Physical Review Letters*, vol. 95, pp. 095504, August 2005.

[58] L.E. Helseth, "Focusing of evanescent vector waves," *Optics Communications*, vol. 283, pp. 29–33, 2010.